LOCALIZED FIRE IN A GALLERY: MODEL DEVELOPMENT AND VALIDATION

*Salmon Fabien[1], Lacanette Delphine[1], Mindeguia Jean-Christophe[1], Sirieix Colette[1], Bellivier Axel[2], Leblanc Jean-Claude[3], Ferrier Catherine[4]
[1] Université de Bordeaux, UMR CNRS 5295 I2M (16 avenue Pey Berland, Pessac, France)
[2] Laboratoire Central de la Préfecture de Police (rue de Dantzig, 75075 Paris, France)
[3]Université de Toulouse, UMR CNRS 5608 TRACES (Allées Antonio Machado 31058 Toulouse, France)
[4]Université de Bordeaux, UMR CNRS 5199 PACEA (Bâtiment B8 Allée Geoffroy Saint Hilaire Pessac, France)
*Fabien.Salmon@u-bordeaux.fr - 0540002706

Keywords: Localized wood fire; Large eddy simulation; FireFOAM; Underground; Toxicity; Rock art cave

ABSTRACT

A numerical simulation of a wood fire in a natural gallery is compared with experimental data. Temperatures, velocities, gases and particles concentrations as well as soot deposits are the measured quantities of the experiment. We expose in this article the comparison with a simulation performed by the open-source solver FireFOAM. In order to improve the accuracy of the modeling, the initial numerical tool has been modified. A boundary condition for temperature based on energy conservation has been added to better estimate thermal losses at the walls. A hypothesis regarding vertical velocity in a confined geometry containing a localized fire is also made. By assuming that the velocity is exclusively horizontal, the error between simulation and experiment is reduced. With the aim of comparing the temperature measurements with the simulation accurately, the thermocouple model commonly used in FireFOAM has been changed. The limitations of the previous models are also discussed. Then, two combustion side issues are presented. First, the model of Beresnev-Chernyak computes soot deposit on walls. Second, the fractional effective doses (FED) for toxicity, radiation and heat hazards have been implemented to evaluate the safety of the environment during the fire.

Nomenclature

a	Absorption coefficient (m^{-1})
C	Concentration (% or ppm)
c_p	Specific heat at constant pressure ($J.kg^{-1}.K^{-1}$)
c_v	Specific heat at constant volume ($J.kg^{-1}.K^{-1}$)
dQ	Power released by the chemical reaction (W)
D	Distance between the fire and the closest wall (m)

F	External force (N)
f	Friction factor
G	Incident radiation ($W.m^{-2}$)
H	Specific enthalpy ($J.kg^{-1}$)
H_t	Total specific enthalpy ($J.kg^{-1}$)
H'	Height of the ceiling (m)
h	Heat convection coefficient ($W.m^{-2}.K^{-1}$)
I	Radiative intensity ($W.m^{-2}$)
k	Subgrid-scale kinetic energy ($m^2.s^{-2}$)
L	Characteristic length (m)
$\dot{m}$	Mass loss rate ($kg.s^{-1}$)
p	Pressure (Pa)
$\dot{Q}$	Heat of combustion ($J.kg^{-1}$)
Q_c	Convective heat release rate (kW)
q_{in}	Incident radiative flux ($W.m^{-2}$)
q_r	Radiative heat flux ($W.m^{-2}$)
R	Ideal gas constant ($J.mol^{-1}.K^{-1}$)
r	Specific gas constant ($J.kg^{-1}.K^{-1}$)
s	Ray direction
S	Source term ($W.m^{-3}$)
S_{ij}	Strain rate (s^{-1})
sr	Stoichiometric coefficient of the oxidizer
T	Temperature (K)
u	Velocity ($m.s^{-1}$)
X	Molar fraction
Y	Mass fraction

Greek terms

Δ	Filter size (m)

ϵ	Emissivity
ϵ_t	Turbulent kinetic energy dissipation ($m^2.s^{-3}$)
ε	Error between simulation and experiment
κ_{eff}	Effective thermal diffusity ($m^2.s^{-1}$)
λ	Thermal conductivity ($W.K^{-1}.m^{-1}$)
μ	Dynamic viscosity ($kg.m^{-1}.s^{-1}$)
μ_{eff}	Effective dynamic viscosity ($kg.m^{-1}.s^{-1}$)
ν	Stoichiometric coefficient
ν_t	Eddy viscosity ($m^2.s^{-1}$)
ρ	Density ($kg.m^{-3}$)
σ	Stefan-Boltzmann constant ($W.m^{-2}.K^{-4}$)
ϕ	Flux ($W.m^{-2}$)
$\dot{\omega}_k$	Chemical reaction rate ($kg.m^{-3}.s^{-1}$)

Subscripts

f	Fuel
g	Gas
k	Specie
o	Oxidizer
x	First cell within the wall
w	Wall
∞	Surrounding

1 Introduction

The fire research has known important changes with the beginning of CFD (Computational Fluid Dynamics) simulation. Nowadays, the advances of numerical simulation with the increasing computing capacities allow the reproduction of real fires. The quality of the numerical representation can be discussed and the complexity of combustion problems is still an important obstacle. The mixing of several physics is the main difficulty for CFD simulation. Turbulence, chemistry and radiation make combustion hardly predictable. CFD tools are currently used in different subjects within the general topic of combustion. For instance, a lot of investigations about LES (Large Eddy Simulation) simulation of

compartment fires were conducted [1], [2], [3]. The authors managed to predict the behavior of fires thanks to numerical simulation. Close to these researches, this study handles the large eddy simulation of fires inside confined geometries. More particularly, this investigation concerns localized fires in gallery-like geometries. Basically, this matter falls within various fire fields such as fire safety in specific confined places like parking lot, underground mining or tunnels. Spread of fire as well as smoke circulation in parking lot is an important issue for people security and the risk of death for people in such public areas has to be estimated. This question was treated by numerical simulations in [4], [5]. The general problem of fires in tunnels is also prominently featured. The safety matter is obviously an old topic [6], [7], that CFD renewed [8], [9]. The storage of hazardous waste in confined places necessitates also caution because of fire risks [10]. This investigation has also links with flames beneath confined ceilings which are broadly studied experimentally and numerically [11], [12], [13]. Besides these contemporary matters, fires in gallery-like geometries can also be a prehistorical issue. For instance, the Paleolithic Chauvet-Pont d'Arc cave [14], [15] contains three kinds of witnesses of prehistorical fires: red colorations of stone areas [16], spallings and soot deposits. These evidence suggest that fires were carried out deep inside this cave between 37,000 and 33,500 years ago [17], [18]. Standard explanations can be suggested such as lighting, ignition source for torches or pigment production [19]. But the unusual scale of the fires in the confined Megaloceros gallery whereas the big Hillaire Chamber could have hosted them leads to other assumptions such as protection from animals or more symbolic functions. For conservation reasons, only numerical simulation can answer to this question. Simulation aims at providing information about the fires function by estimating the amounts of wood, the fire numbers and the ability to supply the hearths despite temperature and toxicity. More broadly, this modeling takes part in the study of the prehistoric Man's appropriation of the underground environment.

First, an experiment was carried out for the purposes of reproducing similar thermal alterations to the ones in the Chauvet-Pont d'Arc cave. A hearth was placed within a former limestone quarry described in the next section. Three fires (one per day) were made in order to test the reproducibility of this kind of combustion. The fire remained localized and no propagation occurred during the combustion. The experimental protocol is detailed in the following section. It should be noted that the quarry, like whichever caves, has an irregular geometry involving unusual difficulties in the numerical resolution. Because we are interested in the reproduction and the simulation of thermal marks, we must use the exact geometry of the quarry with all irregularities.

From this perspective, a previous study [20], linked to the Chauvet-Pont d'Arc fires, was performed with the software FDS [21]. The geometry was simplified for the simulation of weak fires close to a flat wall. The approximation did not impact the numerical results for this kind of fire. However, since the final application of this investigation is the Chauvet-Pont d'Arc cave, the preliminary results of this article aim at validating the model on the exact quarry geometry. Among free open-source software, FireFOAM [22], a tool developed by FM Global, can simulate combustion in any geometry. This solver is then selected to simulate the experimental fire.

Second, the numerical model of FireFOAM is described. It is an OpenFOAM [23] solver dedicated to fire simulations. This open-source software is a very promising tool allowing LES simulations and resolution of aerothermochemistry equations as well as radiation. The flames field is broadly studied with FireFOAM [24], [25], [26]. FireFOAM manages the simulation of fires in confined geometries as demonstrated in [27], [28]. OpenFOAM can also perform calculations in complex geometries which is a key point in this study. Its useful framework for personal C++ programming gives the possibility of implementing additional code. In particular, some general theoretical hypotheses have already been tested in other articles like [29] thanks to the modification of a former version of FireFOAM.

Third, several unavailable features in the version 4.0 of FireFOAM have been added to improve the physical description of fires. We present modifications concerning thermocouple correction, resolution of temperature boundary condition in the case of convection along a wall, and an assumption of an exclusively horizontal velocity far enough from the fire. The latter is a hypothesis that allows FireFOAM to reach better results for this study. Additionally, the deposition of soot during a wood fire and the hazard assessment due to toxicity, temperature and radiation are modeled.

Fourth, details about the numerical simulations are given. Especially, the reconstructed 3D geometry of the experimental cave is presented. Careful choices required for simulation with FireFOAM are also discussed. Lastly, the simulated results are faced with the experimental measures (temperature, velocity, gases and particles concentration). A validation of the numerical heat release rate (HRR) is also achieved in a dedicated section.

2 Description of the fire experiments

2.1 Compartment geometry and fire characteristics

The experiments took place in a former rupelian limestone quarry, located in Lugasson (France). The L-shaped quarry is composed of two right-angle galleries of 9 meters. The entrance in the first gallery leads to the outside (Fig. 1). Because the quarried limestone was used in the Bordeaux building construction, the quarry has the typical dimensions of mine galleries. Keeping in mind the archeological matters [30], a major factor in the choice of the location was the dimensions which are similar to the Megaloceros Gallery in the Chauvet-Pont d'Arc cave. Even if the fire was designed for archeological applications, the combustion consists in a general localized fire.

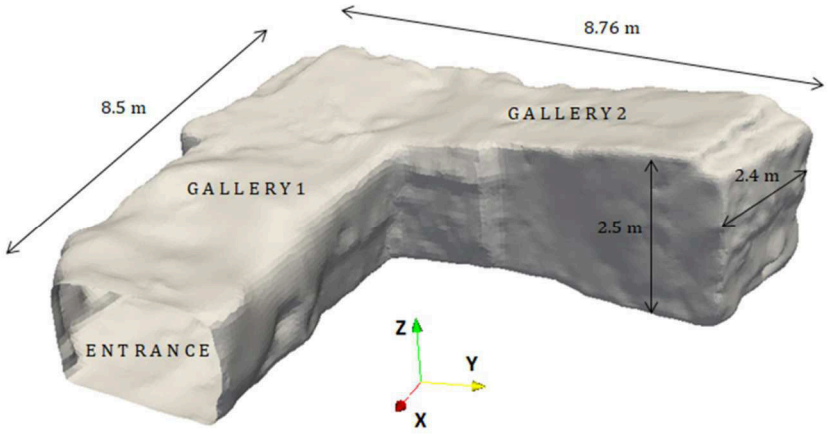

Fig. 1. 3D geometry of the quarry acquired by photogrammetry (P. Mora, Archéotransfert).

The objective of the experiment was the reproducibility of one localized fire. One fire per day was made over three days at the back of the gallery 2. The fireplace was located at 80 cm from the back of the second gallery and centered between both walls. Its diameter was about 80 cm throughout the combustion of the three fires (Fig. 2). The entrance was large enough to ensure the ventilation of the fire.

As regards the fuel, scots pine (pinus sylvestris) was burned. We chose to shape bundles in order to quantify the amount of wood precisely. Each bundle weighted about 4.5 kg. The initial moisture content of the bundles was measured before the tests by a humidity sensor and estimated to be about 22%. The bundles were all composed of branches with typical diameters of the population of scots pine. Each branch had a length of about 80 cm. So, the bundles were all similar and well characterized.

At the beginning of each fire, 4 bundles were put on the burning site to initiate combustion (Fig. 2). According to tests achieved before the experiments [31], a tepee configuration produces a tall flame and optimizes the ceiling jet flow. To maximize the ceiling impact and produce thermo-alterations similar to the thermal marks visible in the Chauvet-Pont d'Arc cave [19], [14], the tepee arrangement was adopted (Fig. 2). The ignition of the 4 first bundles was done with a blowtorch. Then, the bundles were progressively added in pairs to the fire. In total, 30 wood bundles were burned per fire, representing about 135 kg of pinus sylvestris. Because of the extreme conditions, the firewood was brought to the hearth by firemen with security equipment at regular intervals (Fig. 2). The moment of each supply was chosen during the first fire, in order to prevent as good as possible any decay of the heat release rate (Tab. 1). The same supply times were used for the two other fires to have the same protocol.

Fig. 2. On the left: Initial hearth in a tepee configuration at the back of the gallery 2. The wood is placed on a weighing scale. On the right: Wood supply by firemen with security equipment.

Moment (min)	0	6 :28	10 :21	14 :40	17 :36	22 :52	25 :25
Mass (kg)	17.14	9.53	8.51	9.02	8.7	8.42	9.63
Moment (min)	28 :00	31 :10	34 :06	37 :26	39 :27	41 :29	42 :55
Mass (kg)	9.38	9.6	9.27	8.86	8.88	8.65	8.37

Tab. 1. Moments of supply and corresponding added masses.

2.2 Instrumentation

The galleries were instrumented with thermocouples trees, gas concentration sensors (oxygen, carbon monoxide and carbon dioxide), velocity sensors, pegasor particle sensors (soot concentration) and a weighing scale under the hearth. The locations of all the sensors are specified on the figure 3. The weighing scale permited to know the mass of wood burned during the experiment. The mass loss rate is therefore known and the heat realease rate (HRR) is deduced from the heat of combustion. The heating value was estimated to be about 12.5 MJ/kg from a previous calorimeter hood test [31] and is supposed to remain constant during the experiment.

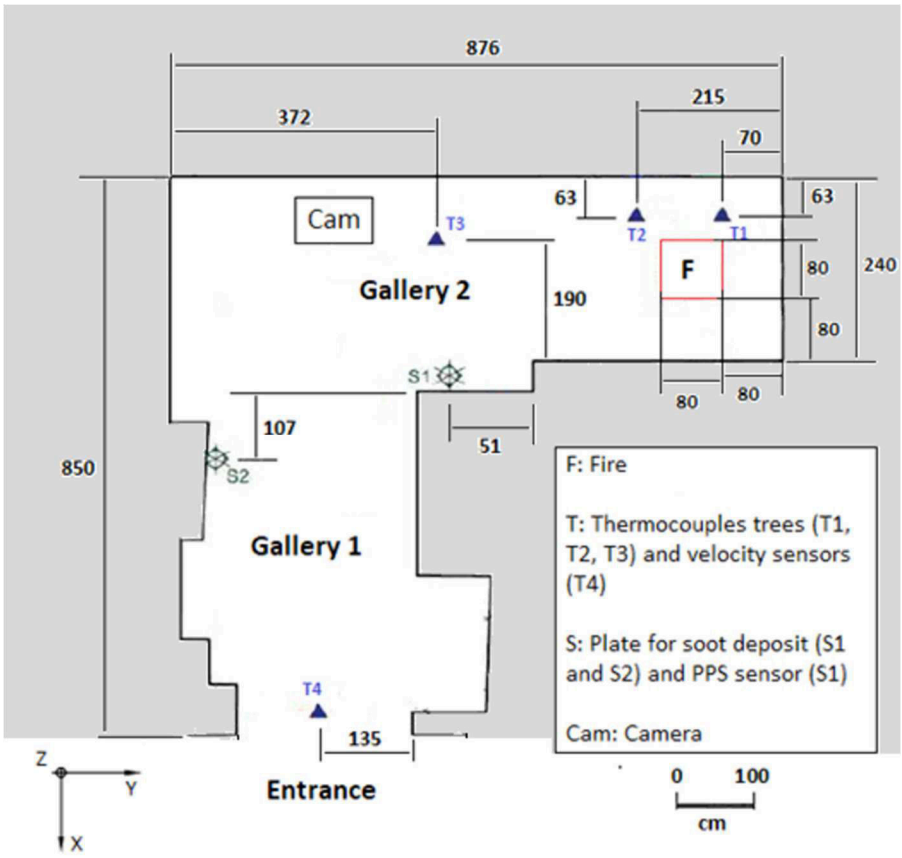

Fig. 3. Cut-away view of the quarry with the locations of the hearth, the thermocouples trees and the soot deposit measures. A camera was placed on the floor, near the corner. Dimensions are in cm.

The thermocouples were positioned in order to have a homogeneous spatial distribution in the fire gallery (trees T1, T2 and T3) and also a uniform vertical dispatching to measure temperature within the cold and hot layers (the exact vertical position of the thermocouples is given in the section 6). Eight 0.5 mm diameter type-K thermocouples were used for the experiment. As they are shielded thermocouples, they are sparsely affected by radiation. The gas sensors measure the concentration of the three gases (oxygen, carbon monoxide and carbon dioxide) at the tree T3, 23 cm under the ceiling. A pegasor particle sensor (PPS) was situated in the smoke at the point S1, 18 cm under the ceiling. It is based on an electrical measure linked to the particle concentrations (supposed soot). The standard calibration [32] is corrected for this kind of soot [33]. We set up the velocity sensors at the entrance of the quarry (T4). An ultrasonic anemometer was fixed at 70 cm above the floor and a McCaffrey probe was fixed at 21 cm under the ceiling. Finally, some aluminum plates were fixed on the walls (points S1 and S2) to collect soot particles and estimate the mass of soot deposited by the thermophoresis phenomena. Located in the corner of the cavity, a camera filmed the experimental fires.

3 Numerical description

In this section, the mathematical equations implemented in FireFOAM-4.0 are detailed. The governing equations are first explained. Then, the turbulence, combustion and radiation models are described.

3.1 Governing equations

FireFOAM solves the Favre averaged Navier-Stokes equations in addition to the Favre averaged transport equations for species mass fraction:

$$\begin{cases} \partial\,\bar{\rho}/\partial t + \partial\bar{\rho}\,\widetilde{u_i}/\partial x_i = 0 \\ \partial\bar{\rho}\,\widetilde{u_i}/\partial t + \partial/\partial x_j\left(\bar{\rho}\widetilde{u_i}\widetilde{u_j}\right) = -\partial\,\bar{p}/\partial x_i + \partial/\partial x_j\,\mu_{eff}\left(2\overline{S_{ij}} - 2/3\,\overline{S_{kk}}\delta_{ij}\right) + \bar{F}_i \\ \partial\bar{\rho}\,\widetilde{H_t}/\partial t + \partial/\partial x_j\left(\bar{\rho}\widetilde{u_j}\widetilde{H_t}\right) = \partial/\partial x_j\,\bar{\rho}\kappa_{eff}\partial\,\widetilde{H}/\partial x_j + \partial\,\bar{p}/\partial t + \partial\,\overline{q_{rj}}/\partial x_j + \overline{F_j u_j} + \bar{S} \\ \partial\bar{\rho}\,\widetilde{Y_k}/\partial t + \partial/\partial x_j\left(\bar{\rho}\widetilde{u_j}\widetilde{Y_k}\right) = \partial/\partial x_j\,\bar{\rho}\kappa_{eff}\partial\,\widetilde{Y_k}/\partial x_j + \bar{\omega}_k \\ \bar{P} = \bar{\rho} r \tilde{T} \end{cases} \quad (1)$$

where $\bar{}$ is the Reynolds average symbol, $\tilde{}$ is the Favre average symbol, ρ is the fluid density, u is the velocity, p is the pressure, μ_{eff} is the effective dynamic viscosity, $\overline{S_{ij}} = 1/2\left(\partial\,\widetilde{u_i}/\partial x_j + \partial\,\widetilde{u_j}/\partial x_i\right)$ is the strain rate, F is the gravity force, H_t is the total specific enthalpy, H is the specific enthalpy, κ_{eff} is the effective thermal diffusivity, q_r is the radiative heat transfer, S is a source term, Y_k is the mass fraction of the specie k, ω_k is the chemical reaction rate, r is the universal gas constant divided by molar mass and T is the temperature.

The unity Lewis number assumption is made. The mass diffusion coefficient is supposed to be equal to the thermal diffusion coefficient. This approximation is a current hypothesis in fire numerical simulation that comes close to the mass transfer reality [21]. The turbulent fluxes of species and total enthalpy are simplified and assumed to be gradients. For instance, regarding the species: $\bar{\rho}\widetilde{u_i''Y_k''} \approx -\bar{\rho}\kappa_{eff}\partial\,\widetilde{Y_k}/\partial x_i$.

The specific heat capacities are estimated thanks to the Janaf thermochemical tables corresponding to polynomial approximations [34]. The thermal conductivities are calculated by the modified Eucken correlation [35]: $\lambda = \mu c_v(1.32 + 1.77\,R/c_v)$ with c_v the specific heat capacities at constant volume. The dynamic viscosities are calculated by the Sutherland's law [36]: $\mu = A_s\,(1 + T_s/T)/\sqrt{T}$, with A_s and T_s two Sutherland's law coefficients.

Then, the fluid properties are calculated for the mixture as molar averages of all species.

3.2 Turbulence modeling

The numerical simulation is based on the Large Eddy Simulation (LES) model. A one-equation turbulence model [37] is used to close the previous set of equations (1). FireFOAM determines the subgrid-scale kinetic energy k by solving:

$$\begin{gathered} \partial\rho\,k/\partial t + \partial\rho\widetilde{u_j}\,k/\partial x_j - \partial/\partial x_j\left[\mu_{eff}\partial\,k/\partial x_j\right] = \\ -2/3\,\rho k\partial\,\widetilde{u_k}/\partial x_k + \mu_{eff}\partial\,\widetilde{u_i}/\partial x_j\left(2\overline{S_{ij}} - 2/3\,\overline{S_{kk}}\delta_{ij}\right) - C_\epsilon\rho\,k^{3/2}/\Delta \end{gathered} \quad (2)$$

where Δ is the filter size directly linked to the cell size and $C_\epsilon = 1.048$. Then, the calculation of the eddy viscosity is computed by $\nu_t = C_k\sqrt{k}\Delta$ with $C_k = 0.094$.

To estimate the eddy thermal diffusivity, we assume that the turbulent Prandtl number is constant and is worth 0.85 (value usually used and deduced from experimental data).

3.3 Radiation Modeling

FireFOAM assumes that turbulence does not affect radiation. Therefore, the radiative transfer equation (RTE) is solved without turbulence interaction. Moreover, the gases are supposed to be a grey medium and scattering is neglected because of the low experimental soot concentration (Fig. 19). The solved radiation equation is not dependent on the spectral properties of gases. With these hypotheses, the radiation equation is:

$$s.\nabla I(r,s) = a(r)\big(\sigma T^4(r)/\pi - I(r,s)\big) + S(r) \quad (3)$$

where I is the radiative intensity, s is the ray direction, a is the absorption coefficient of the medium and $\sigma = 5.67.10^{-8} W.m^{-2}.K^{-4}$ is the Stefan-Boltzmann constant. The term S corresponds to the radiative emission from combustion which cannot be simulated directly because the grid cells are too coarse to estimate correctly local temperatures in the flames. Since the emission term is proportional to the fourth power of temperature, the simulation yields poor results in the flame region. To fix this issue, a source term depending on the heat release rate is usually added in simulations: $S = 0.3dQ$ where dQ is the released chemical reaction power in OpenFOAM. We consider that 30% of the combustion energy is released by radiation for scots pine [38]. The absorption coefficient is estimated by the RADCAL model [39]. Soot radiation is embedded in the absorption coefficient through an additional term [40]: $a_{soot} = B\rho_{soot}X_{soot}[1 + C_{soot}(T - 2000)]$ where ρ_{soot} is the soot density, X_{soot} is the molar fraction of soot, $B = 1232.4 m^2.kg^{-1}$ and $C_{soot} = 4.8.10^{-4}K^{-1}$.

Radiation is solved by the finite volume discrete ordinary method (fvDOM in FireFOAM). The radiative equation is solved in N directions in order to scan all the space (N is given in §5.4).

Concerning boundary conditions, walls are considered as grey diffusive with an emissivity $\epsilon = 0.95$. The radiative intensity is computed as follows: $I_w = \epsilon\sigma T^4 + (1-\epsilon)/\pi \int_{s.n<0} I\, s.n d\Omega$ with n the normal to the face.

3.4 Combustion modeling

It is necessary to model the chemical reaction rate appearing in the species equations and the energy equation. Because we are interested in the global results rather than an accurate flame description, the Magnussen model (Eddy-Dissipation Concept) [41] is sufficient:

$$\dot{\omega} = -\rho C_c\, \epsilon_t/k\, min\big(Y_f, Y_o/sr\big) \quad (4)$$

where the indices f and o denote the fuel and oxidizer respectively, sr is the stoichiometric coefficient of the oxidizer, ϵ_t is the subgrid-scale kinetic energy dissipation, k is the subgrid-scale kinetic energy and C_c is a model constant. To ensure a correct heat release rate,

numerical tests end up at $C_c = 20$. Then, the chemical reaction rate for each specie is $\dot{\omega}_k = \nu_k \dot{\omega}$ with ν_k the stoichiometric coefficient of the specie k.

The chemical reaction of wood combustion is very difficult to figure out. Pragmatically, we choose a reaction that gives coherent results in comparison with the experiment:

$$Wood + 0.4028\, O_2 + 1.516\, N_2 = 0.3609\, CO_2 + 0.8647\, H_2O + 0.0084\, CO + 1.516\, N_2$$

This equation is constant during the combustion. In OpenFOAM, the stoichiometric coefficient of soot is separated from the others and neglected in the calculations of the gases mass fractions. The soot modeling description is detailed in the following section.

3.5 Soot modeling

The soot mass fraction is not computed like the other species. Instead of solving a transport equation, FireFOAM assumes that the amount of soot is proportional to the carbon dioxide quantity. To specify the proportional constant, it uses the following relation: $Y_{soot}/Y_{soot,max} = Y_{CO2}/Y_{CO2,max}$ where $Y_{soot,max}$ and $Y_{CO2,max}$ are both calculated under the assumption that all the fuel is burned in stoichiometric proportions. This simple equation is not time-consuming and is efficient enough for the study. Like gases, the stoichiometric coefficient is chosen to deliver consistent results: $\upsilon_{soot} = 0.0015$.

4 Numerical contributions

This section introduces additional models implemented in OpenFOAM-4.0 to carry out the simulation of the experiments (§2.1).

4.1 1-D heat conduction in a virtual wall

The fire is located within a gallery and a sizeable part of the energy is lost through the walls. In order to consider this phenomenon, we implement in OpenFOAM-4.0 a boundary condition which requires the resolution of the 1-D heat conduction equation for each boundary face. The interface temperature derives from the heat flux balance:

$$q_r + h\left(T_g - T_w\right) = \lambda\,(T_w - T_x)/dx \tag{5}$$

with h the convective heat transfer coefficient, λ the thermal conductivity of the rock and dx the first spatial step discretization in the wall. The indices g,w and x correspond to the gas, wall surface and first discretization in the wall respectively. The model must account for the water in walls because they were saturated [42]. The evaporation of water is modeled through a high value of the specific heat capacity at 100°C [43], [20].

The convective tranfer corresponds to the loss due to boundary layers. Modeling them requires millimeter-sized cells in the parallel direction of the wall to catch the little irregularities. Then, because of the large geometry, the mesh of boundary layers necessary for wall-resolved LES would demand time-consuming computations. Moreover, the input geometry file (built by photogrammetry) is not precise enough to include such irregularities. Therefore, wall-resolved LES is not feasible in this study.

So, the convective heat transfer must be modeled by empirical formulations. It is usually used in CFD simulations, for instance in FDS [21]. However, this approach highly depends on the first discretization at boundaries. The convective heat transfer coefficient should be estimated with the properties of the gas outside the boundary layer. In the simulation, we assume that the temperature of the first cell center approximates the gas temperature outside the layer. Then, this method is grid-dependent but a finer discretization would not necessarily provide more reliable results because the needed temperature must stay outside the boundary layer. Therefore, the safer approach in this specific case is the use of empirical formulations adapted to the experimental data.

The ceiling jet phenomenon prevents the application of Nusselt number correlations to the ceiling. Instead, the Alpert correlation $h = 0.246 f (Q_c/H')^{1/3} \dot{} (\mathrm{r}/H')^{-0.69}$ is used [44]. r is the radial distance from the fire, H' is the height of the ceiling above the fireplace, Q_c is the convective heat release rate and f is an empirical friction factor. This formulation is only valid while $0.17 < r/H' < 4$. In the turning region ($r/H' < 0.17$), the convective heat transfer remains constant. For smooth plate unconfined ceilings, $f = 0.03$ gives satisfying experimental results but the simulation requires another value. The figure 4 displays qualitatively the differences between simulated and theoretical gas temperatures along the first cells near the ceiling [44]. The grid cells are too coarse to capture the increase of temperature a few centimeters under the ceiling. Then, the temperature T_g in (5) is underestimated by the simulation as shown on Fig. 4. Therefore, the convective heat transfer coefficient must compensate for this underestimation. Considering these explanations, the best fit to the data leads to a subgrid-scale friction factor $f_{sgs} = 825$. This correlation is applied to the ceiling until 2.7 m from the fire centerline, respecting the validity range.

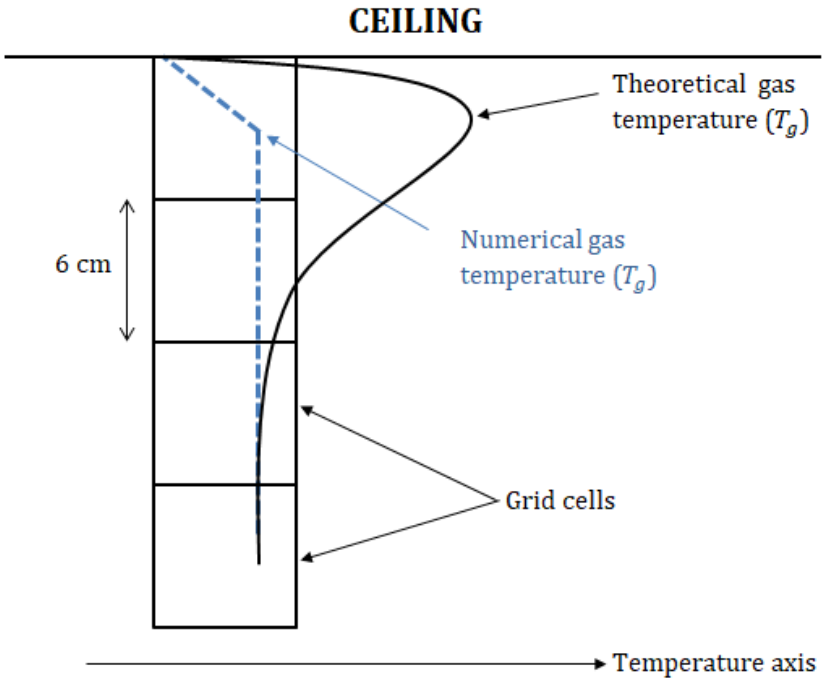

Fig. 4. Comparison between theoretical and simulated temperature profiles close to the ceiling.

The convective heat transfer coefficient for walls is usually estimated from the Nusselt number correlations for planes [45]. Then, $h = Nu\,\lambda/L$ with Nu the Nusselt number and L a characteristic length corresponding to the boundary layer length. A characteristic length of 1 m is often applied in fire simulators (FDS for instance [21]). However, for enclosure fires, negative buoyant wall flows can happen [46]. This physical process (Fig. 5) occurs when walls are close enough to the fire ($D < H'$). Then, inertial forces can be stronger than buoyancy forces and downward wall flows can appear. The quarry is 2.4 meters wide ($D =$ 1.2 m) and 2.5 meters high at the fireplace so this gases circulation took place during the experiment.

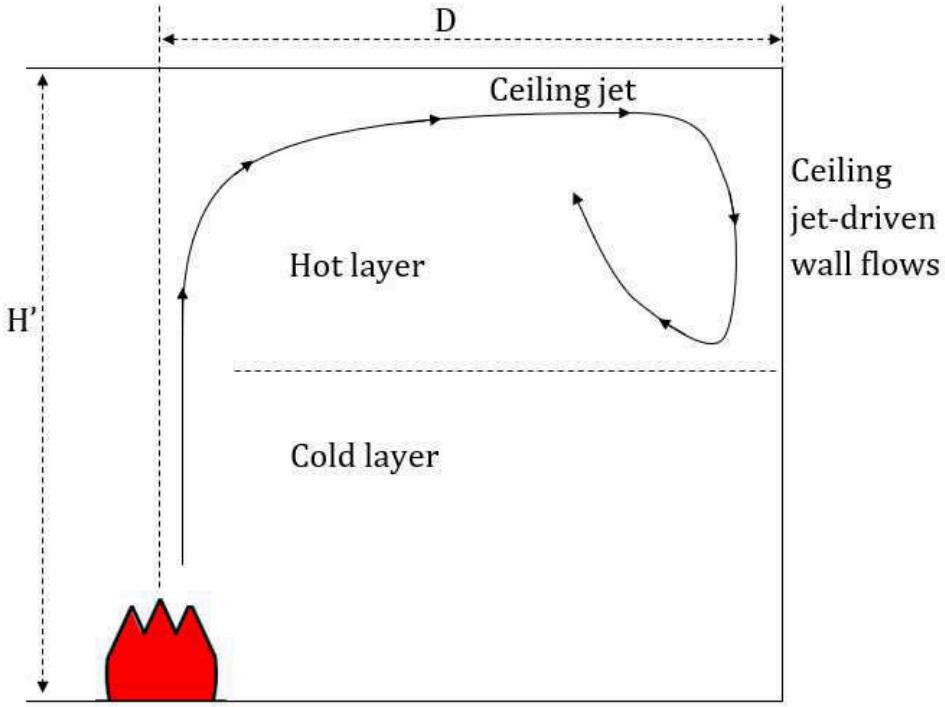

Fig. 5. Schematic representation of the ceiling jet-driven wall flows phenomenon (without penetration in the cold layer).

Cooper in [47] and [48] showed that the ceiling jet-driven wall flows can go down up to 80% of the ceiling height. Therefore, the temperature close to walls is higher than in the hot layer. Again, the coarse grid does not allow accurate calculations of the temperature near walls. A subgrid-scale modeling has to be set up for the characteristic length.

The characteristic length must depend on layers. In the cold layer, the same characteristic length as FDS is chosen: 1 m. In the hot layer, the value of the subgrid-scale characteristic length is taken at 0.1 mm to make the simulation values fit the experimental ones.

A critical temperature of 400 K is chosen to distinguish the hot layer from the cold layer because this value gives consistent results. Nevertheless, it seems that the precision of this temperature is not very important when the hot layer temperature is far higher than the cold layer temperature.

4.2 Soot deposit

A thermophoresis model has been added to compare the experimental and numerical soot deposits. Thermophoresis is usually considered as the dominant process responsible for the deposition of soot particles on vertical walls when the temperature gradient between gases and solids is important. The motion source of particles is then the temperature gradient in the mixture of gases. In a hot surrounding gas, collisions are more important than in a colder gas. As a result, soot particles migrate to the colder surroundings, so partly to the walls. The thermophoretic velocity is defined by: $V_{th} = -K_{th}\,\mu_g/\rho_g\,\nabla T/T_g$.

The thermophoretic diffusion coefficient K_{th} has to be modeled. In this study, K_{th} is estimated by the Beresnev and Chernyak model [49] because some studies showed its good agreement with experimental data [50], [51].

4.3 Fractional effective dose (FED)

An essential issue is the toxicity assessment in a confined place. The capability for prehistorical men to stand near a fire in a cave is an important matter as well as the intoxication of trapped people in tunnels or mines. Hence, we set up a living condition modeling with the so-called fractional effective dose (FED). This model evaluates the severity of toxic effects, temperature and radiative hazards. In the simulation, two kinds of FED are calculated. The first one is dedicated to gas toxicity whereas the other one is focused on temperature and radiation hazards. The FED is based on the dose notion, so the more you are exposed to hazard, the more your dose increases without ever reducing. This dose is a time integration: $FED = \int dt/t_{50\%}$, where $t_{50\%}$ defines the required time to kill half of people. Thus, when the FED is worth one, the mortality rate is 50%. The FED of radiation and heat is the sum of both parts. The radiative incapacitation time [52] is $t_{50\%,rad} = 10q_r^{-1.33}$ when $q_r > 2.5\ kW/m^2$ and tends to infinity in the other case ($FED = 0$). The following formula gives the heat incapacitation time [52]: $t_{50\%,heat} = 5.10^{22}T^{-11.783} + 3.10^{7}T^{-2.9636}$. If the temperature is higher than 200°C, the incapacitation time is 0 (anyone dies).

As regards gas concentrations, there are interactions between gases toxicities. The fractional effective dose is as follows [52] [53] [54]: $FED = HV_{CO_2}FED_{CO} + FED_{O_2} + FED_{CO_2}$ with

$$t_{50\%,O_2} = exp\left(8.13 - 0.54\left(20.9 - C_{O_2}\right)\right)$$

$$t_{50\%,CO} = 10^5\ C_{CO}^{-1.036}/2.764$$

$$t_{50\%,CO_2} = \begin{cases} 0 \text{ if } C_{CO_2} < 5.5\% \\ 2193.8 - 311.6C_{CO} - 311.6C_{CO_2} \text{ if } 5.5\% < C_{CO_2} < 7 \\ exp\left(6.1623 - 0.5189C_{CO_2}\right) \text{ if } C_{CO_2} > 7\% \end{cases} \quad (6)$$

$$HV_{CO_2} = exp\left(0.1903C_{CO_2} + 2.0004\right)/7.1$$

where C_k is the concentration of the specie k in % except for carbon monoxide in ppm (parts per million).

4.4 An accurate thermocouple correction

On the one hand, the experimental temperatures correspond to the temperatures given by the measuring sensors (thermocouples). On the other hand, simulation supplies the gas temperatures. But a gap necessarily exists between the gas temperatures and the measures. First, the sensor is solid and can be more affected by radiation than the surrounding gas. Second, a boundary layer occurs at the thermocouple surface and losses by convective heat transfer happen. Thus, a temperature correction is required to compare experimental measures with the simulation accurately. The following discussion handles temperature corrections applicable to general thermocouples.

OpenFOAM already contains a thermocouple correction model [55]. However, we modify it to enhance the correction accuracy. The OpenFOAM model and our modifications are detailed below.

First, the thermocouple is assumed to be thermally thin because its diameter is small enough (0.5 mm in this study). Consequently, the conduction in the sensor is neglected and the temperature in the thermocouple is homogeneous. The energy balance leads to:

$$\rho c_p V \partial T/\partial t = q_r A + h\left(T_g - T\right)A \tag{7}$$

where c_p is the specific heat at constant pressure of the thermocouple, V is the thermocouple volume and A is its area. The radiative heat transfer may be expressed as $q_r = \epsilon(q_{\text{in}} - \sigma T^4)$ with ϵ the thermocouple emissivity.

The key point is the calculation of the incident radiative flux q_{in}. In the existing OpenFOAM model, the incident radiative flux is replaced by the incident radiation $G = \int I\,(r,s)d\Omega$ and the equation (8) is then solved:

$$\rho c_p V \partial T/\partial t = \epsilon(G - \sigma T^4)A + h_{conv}\left(T_g - T\right)A \tag{8}$$

Contrary to this formulation, we decide to compute the incident radiative flux by the exact formula $q_{\text{in}} = \int_{s.n<0} I\,(r,s)s.nd\Omega$ (with n the normal of the thermocouple). Without any information about the thermocouple normal, the incident radiative flux is averaged over the 6 main directions.

To check the efficiency of the implemented model, a simple test case with an analytical solution has been run. Physically, we want to describe the increase in temperature of a cylindrical thermocouple ($\epsilon = 0.9$) located within an empty cubic geometry whose the walls temperature remains at 500 K. The black body assumption for the walls is made. Because the area of the thermocouple is negligible against the box area, the thermocouple temperature is governed by $\rho\frac{d}{4}c_p\,dT/dt = \epsilon\sigma(T_\infty^4 - T^4)$ with $T_\infty = 500\ K$ the surronding temperature, ρ the thermocouple density, d the thermocouple diameter and c_p the thermocouple specific heat capacity. The existing OpenFOAM model, the implemented one and the analytical solution are compared on the figure 6. The equations are solved with $\rho = 8800\ kg.m^{-3}$, $d = 1\ mm$, and $c_p = 440\ J.kg^{-1}.K^{-1}$.

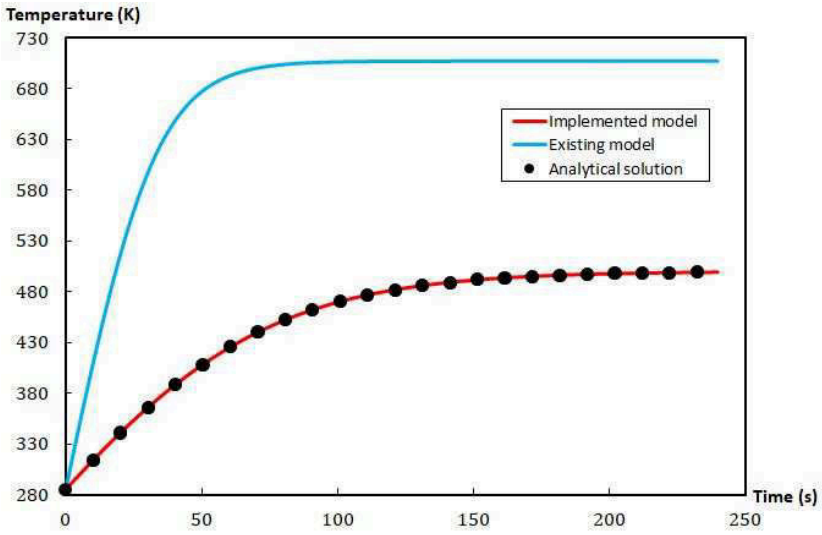

Fig. 6. Evolution of a thermocouple response in a simple test case, calculated with the existing model and the new implemented one. Both models are compared to the analytical solution.

Because the computed value of q_{in} is 3544 W.m^{-2} which is equal to σT_{∞}^{4}, the new model solves the same equation as the analytical theory. The existing model does not give satisfactory results. The value of G given by OpenFOAM is 14175 W.m^{-2}. It is worth noting that in this case, we have the equality $G/4 = q_{\text{in}} = \sigma T_{\infty}^{4}$. This equality can be demonstrated in this simple case but it is not true in general. Nevertheless, some numerical tests have systematically given the approximation $q_{\text{in}} \approx G/4$ with a good precision. Besides, the software FDS uses this approximation to provide thermocouple corrections. Therefore, the existing model could be extended to the one in FDS by replacing G by $G/4$ in the equation (8). Nonetheless, the new model gives more satisfactory and safer results because it is based on mathematical considerations.

All the considerations about the computation of the incident radiation are not applied to the simulation of the experiment because the thermocouples are shielded ($\epsilon = 0$). This assumption means that no radiation occurs between the measuring point and the sheath even if residual radiative fluxes can sometimes exist.

4.5 The horizontal velocity hypothesis

The measurements show that temperature is homogeneous in the hot layer. For instance, the figure 7 displays the temperatures measured in the hot layer at the tree T1. It is worth noting that the temperatures at the points T1_1 and T1_2 are similar despite a 50 cm vertical distance between both thermocouples. This well-known phenomenon has been observed for the three experimental fires.

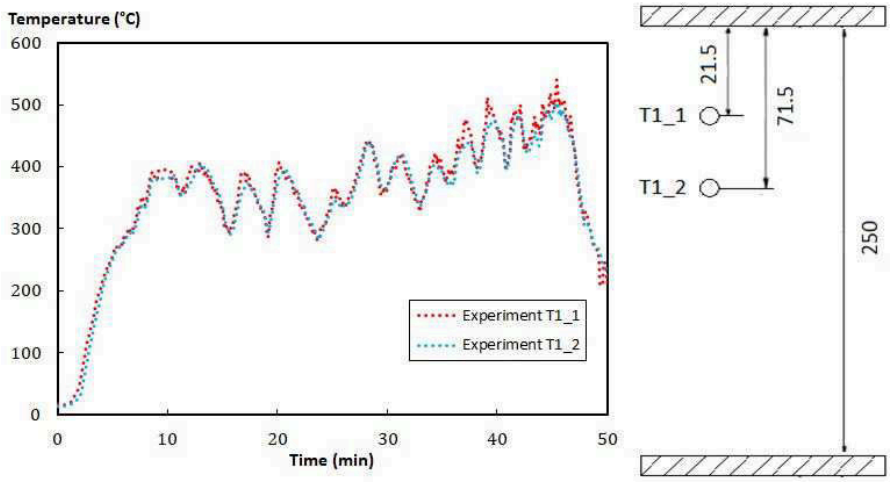

Fig. 7. On the left: measured temperature at the tree T1 at the points T1_1 and T1_2. On the right: cross section of the gallery near the tree T1, showing the vertical location (in cm) of the thermocouples.

Physically, this observation necessarily involves the absence of any energy flux between both points. Therefore, by dividing the flux into the three usual heat transfers (conduction, convection and radiation), we reach the equation: $\phi_{cond} + \phi_{conv} + \phi_{rad} \sim 0$.

There is no difference of temperature between both points so the conduction heat transfer is almost nil. The radiative transfer can be separated into two contributions for each point: the incident and the emitted radiative heat fluxes. We note A and B the two points. So, $\phi_{rad} = \phi_{in,A} - \phi_{em,A} - \phi_{in,B} + \phi_{em,B}$ with $\phi_{em} = \sigma T^4$. Since the temperatures are the same, $\phi_{em,A} \sim \phi_{em,B}$. Furthermore, the incident fluxes cannot be very different from one point to another as long as the distance between them stays relatively small. Consequently, $\phi_{in,A} \sim \phi_{in,B}$. We deduce that the radiative heat flux is worth about zero: $\phi_{rad} \sim 0$. Therefore, the absence of global heat transfer leads to $\phi_{conv} \sim 0$. The subsequent result of this property is the absence of vertical convective transfer between both points. Then, if a vertical velocity exists, a counter velocity is required to balance the flux. But, without any temperature gradient, there is no source of vertical motion because the effects of gravity on the layer are the same at every point. Consequently, only negligible vertical velocities can exist in a homogenous layer.

We point out that the absence of convective heat transfer within hot layers is already used in fire zone models (homogeneous layer temperature assumption), for instance in CFAST [56]. Moreover, there is no convective heat transfer between both layers. In the fire compartment, the only transfer between the layers occurs in the turning region (above the fire) in CFAST.

A simulation of the experiment with FireFOAM-4.0 cannot forecast this behavior. The vertical velocity is not low enough to prevent an excessive convective heat transfer. For little heat release rates (HRR), FireFOAM computes approximately two layers. But in such a confined geometry, the software does not simulate two layers correctly. Instead, a regular temperature gradient takes place as showed on the figure 8.

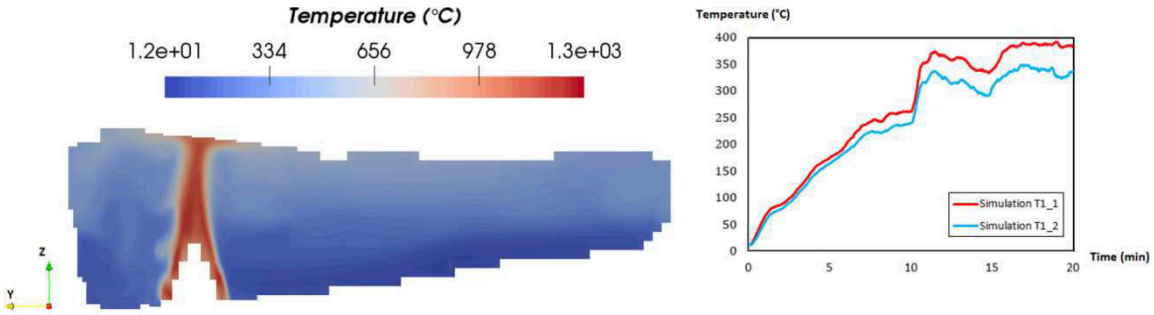

Fig. 8. On the left: numerical temperature field in the median section of the second gallery 20 minutes after the ignition of the combustion. On the right: simulated temperature at the tree T1 at the points T1_1 and T1_2.

Therefore, without enforcing velocity, the temperature profiles do not represent two distinct layers which is not acceptable in this study because it is not the reality. To avoid this major problem, we neglect the vertical convective heat transfer which FireFOAM overestimates. In order to keep the code architecture, we simply force the value of the z-velocity to 0 after each calculation of the velocity. This enforcement is not made in a zone ($r < 0{,}8$) a little greater than the turning region ($r < 0{,}4$). This assumption is schematically represented on Fig. 9.

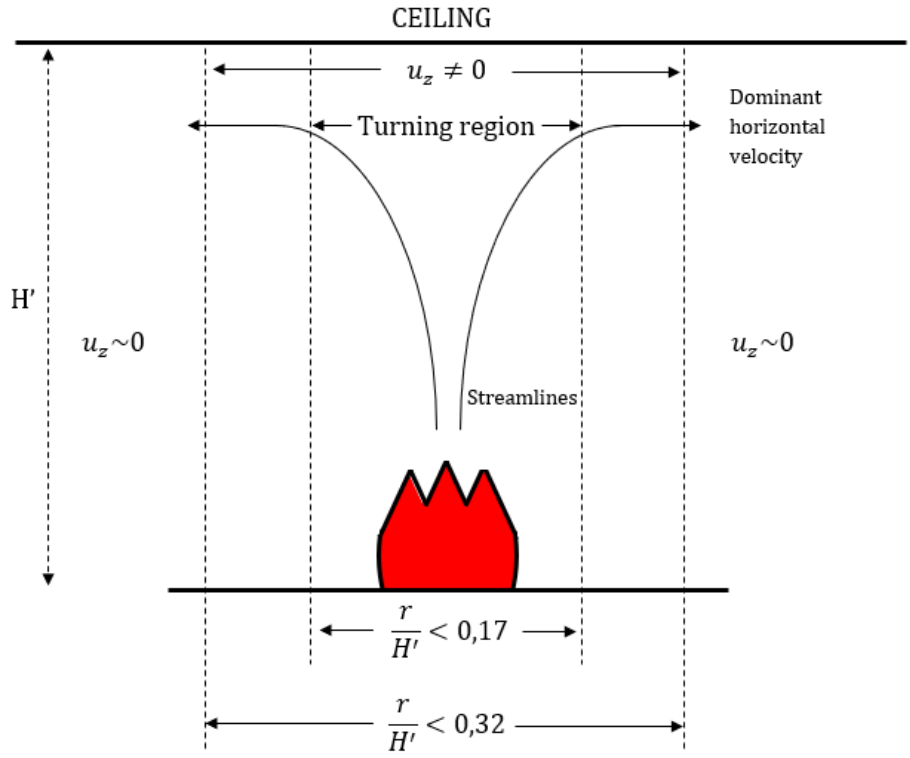

Fig. 9. Schematic representation of the horizontal velocity hypothesis. The enforcement is only applied far enough from the fire.

Moreover, we want to keep simulating the upward convection due to temperature gradient because it is necessary with an irregular ceiling which may have some recesses. Therefore, in

each cell, if the temperature of the cell above is lower, we keep the calculated velocity without enforcing $u_z = 0$. By this way, we authorize the gases to rise in higher recesses.

Now, the gradient is not regular anymore and two layers are simulated by this modified FireFOAM version (Fig. 10). Consequently, the temperature remains almost homogeneous in the hot layer.

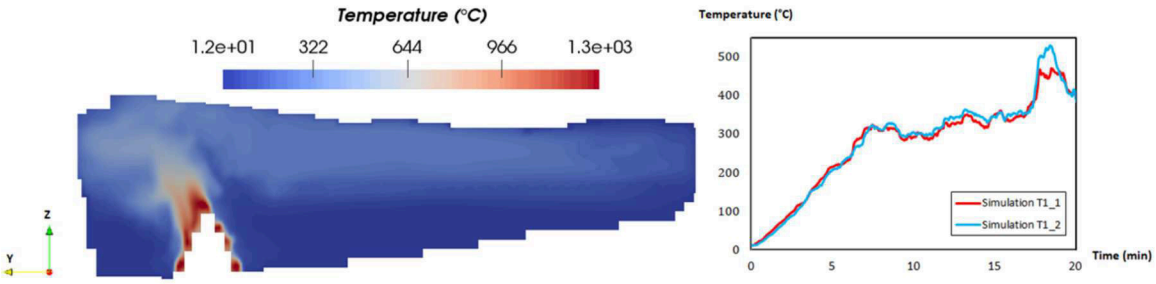

Fig. 10. On the left: numerical temperature field in the median section of the second gallery 20 minutes after the ignition of the combustion. On the right: simulated temperature at the tree T1 at the points T1_1 and T1_2. Both are performed without z-velocity outside the turning region.

The global comparison between experiment and simulation is presented with this assumption in the section 6.

5 Numerical setup

5.1 Geometry mesh

Thanks to photogrammetry techniques, a 3D survey of the quarry has been achieved (Fig. 1). The input file of the simulation thus consists in a CAD file of the quarry. Then, the meshing tool “snappyHexMesh” [57] meshes the geometry with specified size cells. Because of the domain scale and the duration of the fire (50 minutes), choices must be made to mesh the geometry. In this study, we are not interested in describing accurately the flame but rather having an acceptable description of the global environment. The computational domain is meshed with cells of 3 cm above the hearth, 6 cm cells in the hot layer and 12 cm cells in the remainder of the quarry (Fig. 11). The mesh includes about 290,000 cells. A cartesian mesh has been chosen because snappyHexMesh cannot properly manage unstructured meshes with centimeter-sized cells. Moreover, for the purpose of applying this modeling to the more complex Chauvet-Pont d’Arc cave geometry, structured meshes appear safer.

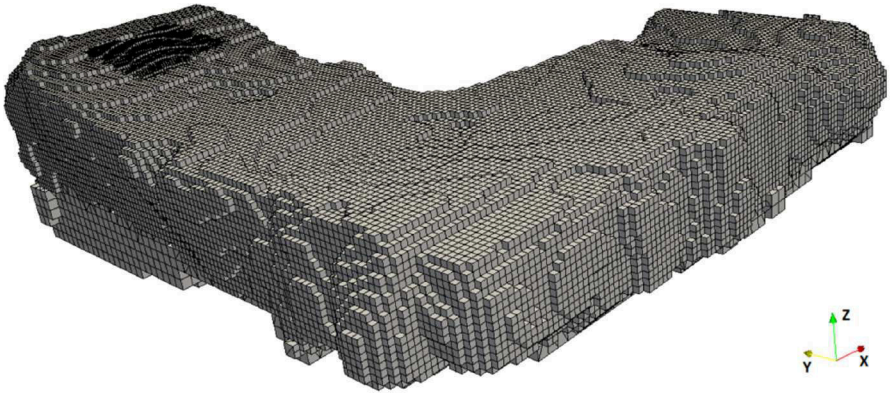

Fig. 11. 3D mesh of the quarry performed by the tool snappyHexMesh [57].

The hearth needs to be present and meshed as a wall in the simulation. Without it, the gases circulation would press the flame against the back of the gallery 2. Because of the sensitivity of FireFOAM, the hearth must be carefully meshed. The real teepee looks like a pyramid (Fig. 12) in the simulation in order to have plate burners numerically more stable.

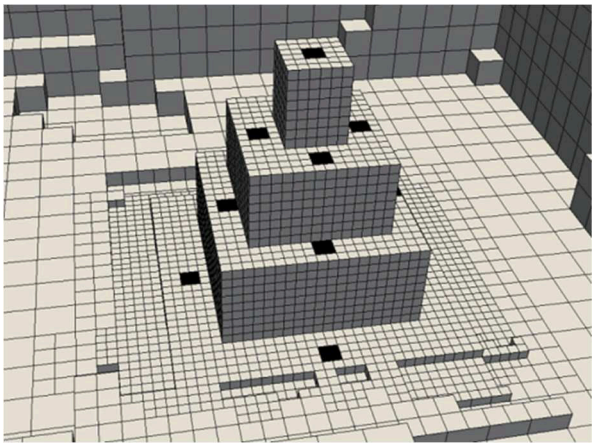

Fig. 12. 3D mesh of the hearth at the back of the gallery 2 with plate burners (black color).

5.2 Heat release rate boundary condition

The HRR is linked to the mass flow rate through the heat of combustion $HRR = \dot{m}\dot{Q}$**.** The mass flow rate boundary condition at the burners corresponds to the measures of the weighing scale. Plate burners are sporadically placed on the hearth (in black on Fig. 12). The mass flow rate boundary condition is only applied to the plate burners. On the rest of the pyramid, the velocity is fixed at 0 (as a wall).

Basically, the heat release rate (HRR) corresponds to the sum of the released chemical powers of all cells. So, a gap can exist between the prescribed boundary condition and the HRR calculated after the resolutions of the set of equations (1) if numerical errors happen. Some numerical tests show that the burner surface has a not expected great influence on the HRR. The surface appears in the computation of the mass flow rate through $\dot{m} = \rho U A_{Burner}$. Because the user specifies the value of the mass flow rate at the boundary, the surface should not affect the value of the HRR. To demonstrate that the contrary happens, a test case

consisting in a square plate burner (in black on Fig. 13) within a cube is run. The mesh only includes cells of 3 centimeters.

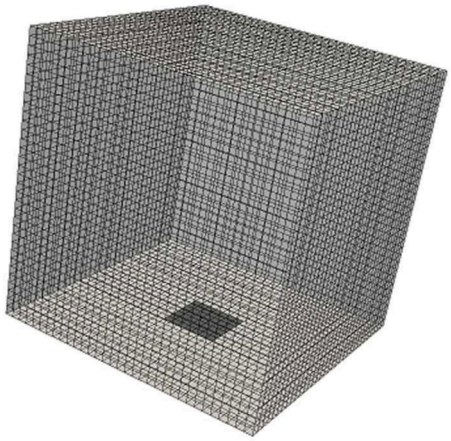

Fig. 13. 3D geometry of the test case corresponding to a cube. The plate burner is the black square (variable size depending on the configuration).

The mass flow rate is fixed at 0.02 kg/s at the burner and the cube walls are adiabatic. The heat of combustion being 12.5MJ/kg, the HRR must be 250 kW. 4 configurations with various areas are inspected (Table 2):

	Configuration 1	Configuration 2	Configuration 3	Configuration 4
Area (cm²)	9 x 9 cm²	21 x 21 cm²	39 x 39 cm²	57 x 57 cm²

Tab. 2. Plate burner areas for each configuration.

The results of all configurations are showed on Fig. 14. The expected HRR should fluctuate around 250 kW for all configurations. This is true for the first two configurations but not for the third and fourth one. To get a consistent numerical HRR, we must use a little area. The larger the area is, the more the numerical HRR is overestimated. Under a critical area, the HRR does not decrease anymore. 21 x 21 cm² configuration seems to be just under this critical area for 3 cm cells and this combustion. This area is chosen in the simulation of the experiment (Fig. 12). For other discretizations and combustions, a critical area still exists but might be different from the configuration 2.

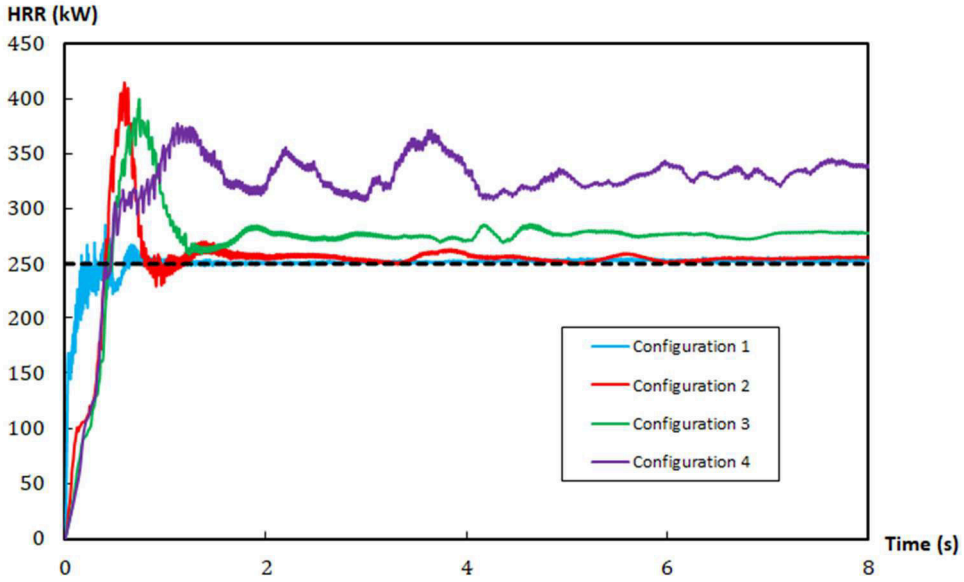

Fig. 14. Comparison between the numerical heat release rates of the four configurations. The dashed line corresponds to the theoretical HRR.

The comparison between the experimental and the numerical HRR is presented in the section 6.1.

5.3 Initial and boundary conditions

The hearth is considered as adiabatic. At the quarry walls, the temperature is calculated by the equation (5). The velocity is fixed at 0 everywhere except at the burners where the HRR is imposed through a velocity boundary condition (§5.2). All mass fractions satisfy zero Neumann boundary conditions at every wall. Outside the gallery, a big volume (20 x 20 x 80 m^3) is added to the quarry geometry to keep a stock of ambient air. At the walls of this volume, the temperature is fixed at 12°C like the initial condition.

5.4 Numerical considerations

Radiation requires the discretization of the space in 32 solid angles. Moreover, the radiative transfer equation (3) is solved once every 10 flow resolutions. Some tests were conducted with more solid angles and more frequent RTE resolutions (equation 3). In this study, both parameters do not have any influence beyond these values.

Finite volumes are used to solve the governing equations (1). The Courant number is limited to 0.6. A more restricted CFL (Courant-Friedrichs-Lewy) condition does not improve the results but a higher Courant number reduce precision.

A decomposition of the domain is carried out in order to parallelize the calculation. 96 cores (8 processors) are used to perform the simulation on a Bullx DLC server with 4 x 24 cores Intel Haswell-EP Xeon 12-Cores E5-2690 V3 2.6 GHz. About 72 hours are needed to compute 50 minutes of combustion.

6 Results and discussion

This section presents the comparison between the experimental measures and the numerical results of the second fire. The comparison is made with this fire for measurement quality reasons. Temperatures, velocities, gas concentrations, soot concentrations, fractional effective doses and soot deposits are the investigated parameters. When it is significant, the average error $\varepsilon = \frac{|v_{exp} - v_{simu}|}{v_{exp}}$ is provided.

6.1 Numerical Heat Release Rate

The numerical HRR is calculated at every time step as the sum of the parameter dQ which corresponds in OpenFOAM to the power released by chemical reactions. The experimental HRR is estimated from the mass flow rate and the assumption that the heat of combustion stays constant with a value of 12.5 MJ/kg. The figure 15 displays the comparison between both.

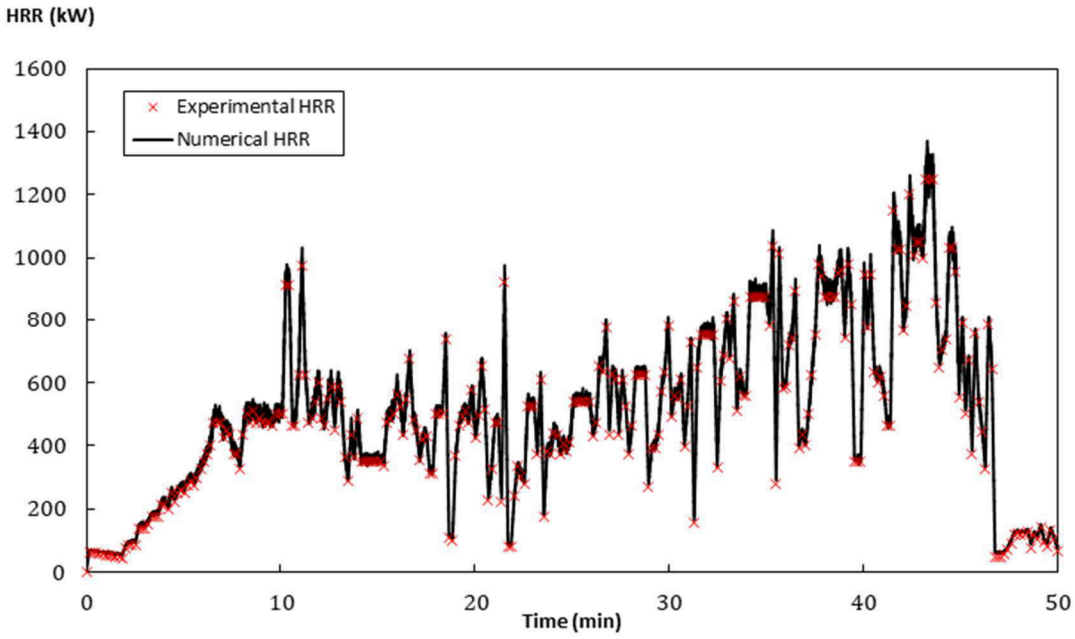

Fig. 15. Comparison between the numerical and the experimental HRR (Heat Release Rates).

Excepting for expected fluctuations, the numerical simulation is totally in accordance with the experimentation. The average error is $\varepsilon < 3\%$. It should be pointed out that we ensured this agreement with the value of the constant model C_c (equation 4) and the decrease of the numerical burner area. But the good trend with all the variations does not only stem from these careful choices. So, it validates the combustion modeling of the simulation.

6.2 Temperature

The simulated temperatures, corrected by the thermocouple model presented in §4.4, are compared to the measured ones for the thermocouples trees T1, T2 and T3 (Fig. 3). As expected, a strong thermal gradient takes place between the hot and cold layers during the main part of the experiment. After the establishment of the convection inside the quarry, the

limit between both depends on the location in the quarry but remains around 1 m from the floor.

The first studied tree is T1. It is close to the fire at the back of the second gallery (Fig. 3). As described in §4.5, the thermocouples T1_1 and T1_2 desmonstrate that the temperature does not change on 50 cm (Fig. 16). Near the ceiling, the temperature exceeds 300°C during more than 40 minutes. The temperature sensor T1_3 is in the cold layer during the main part of the combustion excepting at the end when the existence of two layers can be challenged.

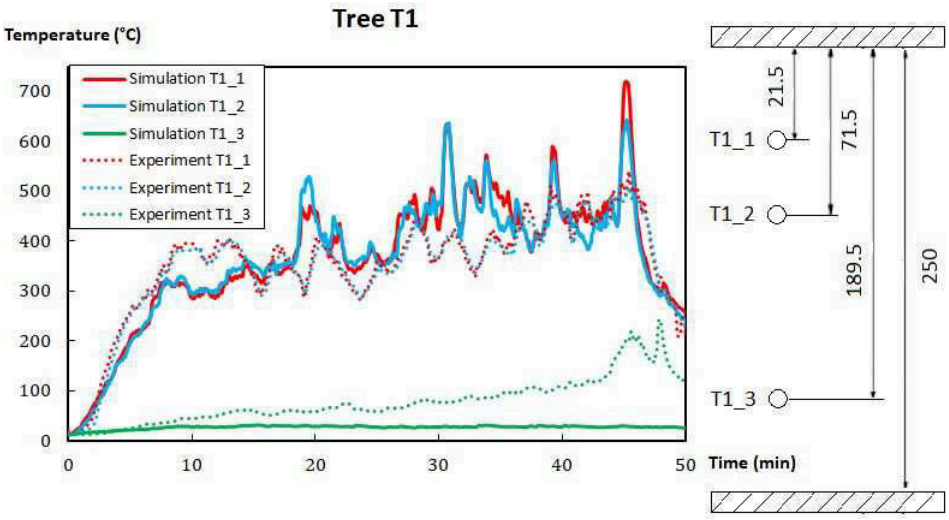

Fig. 16. On the left: comparison between the numerical and experimental temperatures at the tree T1. On the right: cross section of the gallery near the tree T1, showing the vertical locations (in cm) of the thermocouples.

In the simulation, thanks to the hypothesis of an exclusively horizontal velocity (§4.5), the temperature is almost homogeneous in the whole hot layer. Without it, the FireFOAM simulation of this experiment would have given quite higher temperatures in T1_1 than in T1_2. Moreover, the simulated temperature in the hot layer remains very close to the experimental one during the whole time of the fire. The average error for both points is less than 17%. The simulated temperature near the floor (T1_3) is colder than the experimental results, especially at the end of the experiment. It may be essentially due to the horizontal velocity assumption. Close to the fire, the heat transfer from the hot layer to the cold one could be important and the two layers might not be distinctly separated. Thereby, a vertical velocity could be not nil at the boundary between layers. Moreover, as we move away from the fire, the velocity becomes almost exclusively horizontal (Fig. 9). But, the tree T1 might be too close to the fire to consider that the assumption is entirely correct at T1. However, despite the likely excessive aspect of this assumption next to the fire, it yields better results than without it, even for the cold layer.

The tree T2 is also near the fire and the distance from the fire is similar to the tree T1 (Fig. 3). However, this tree is closer to the entrance of the gallery than T1. The experimental temperatures look like those of the first tree but T2_1 is colder than T1_1 (Fig. 17). Because the first tree is trapped between the fire and the back of the gallery 2, the gases are hotter

around the tree T1. The sensor T2_2 comes in the hot layer about 30 minutes after the ignition. The last thermocouple stays in the cold layer and is slightly affected by the fire.

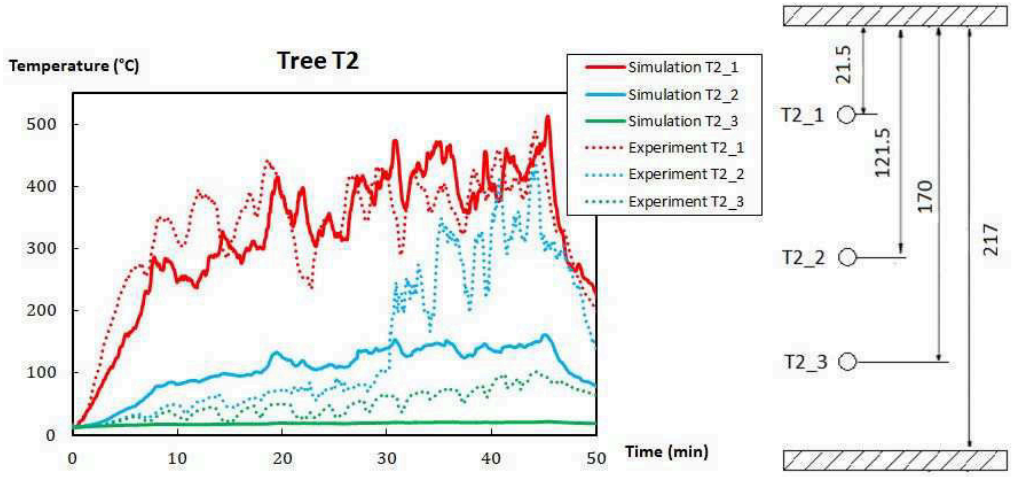

Fig. 17. On the left: comparison between the numerical and experimental temperatures at the tree T2. On the right: cross section of the gallery near the tree T2, showing the vertical locations (in cm) of the thermocouples.

Like the tree T1, the simulated temperature near the ceiling (T2_1) is reliable (average error inferior to 16%). Concerning the two others, the simulation globally underestimates the temperatures. The medium temperature (T2_2) is tough to analyze because this point is somehow between both layers. So, the measured temperature is very different over a few centimeters. The difference of temperature can come only from a little gap between both locations. Nevertheless, like the coldest one, the simulation gives a lower temperature than expected. The previous conclusions about the proximity to the fire can be transposed to this tree. There is not enough heat transfer to the cold layer.

Eventually, the tree T3, which is the farthest from the fire, is analyzed. The comparison is presented on the figure 18.

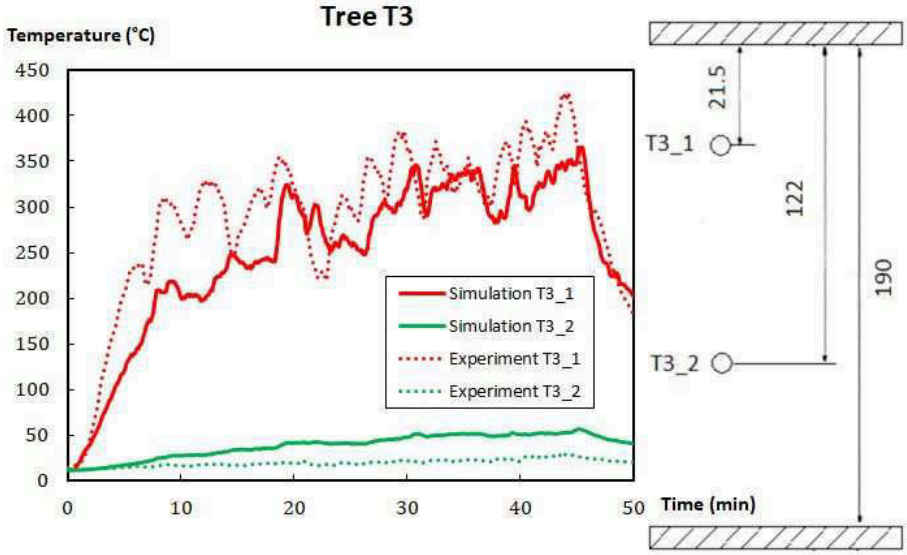

Fig. 18. On the left: comparison between the numerical and experimental temperatures at the tree T3. On the right: cross section of the gallery near the tree T3, showing the vertical locations (in cm) of the thermocouples.

In the cold layer (T3_2), the temperature is not affected by the fire. The simulation is then in accordance with the reality even though a temperature increase dwells until the end of the combustion. But, the error remains acceptable considering that the deviation does not exceed 30°C. In the hot layer, the trend is well described by the simulation and the temperature is very comparable to the experiment. The average error is inferior to 17%. But, the simulated hot layer is slightly colder than the measure, especially during the beginning. The hot layer seems to be too thick in the simulation. The energy is spread out on a larger volume and because it is less concentrated, the upper temperature is too low and the bottom temperature is too high. Even with the assumption of an exclusively horizontal velocity, it turns out to be difficult to compute the thickness of both layers as we move away from the fire. These troubles can be the expression of the accumulation of inaccuracies due to coarse discretization. FireFOAM being very costly, we are limited in the number of cells. And even if some tests were made with finer discretizations without major changes, we cannot rule out this source of error.

6.3 Gases and particles concentration

The gases concentration was measured at the point T3_1 (Fig. 3). Sensors measured the concentration of three gases: dioxygen, carbon dioxide and carbon monoxide (Fig. 19). The dioxygen decreases until about 16% and then oscillates around this value with the wood supply. The carbon dioxide (CO_2) increases until a value of about 5% and stays at this order of magnitude during the fire. This value can cause pathologies if the residence time is too important. The carbon monoxide (CO) increases sharply and reaches a 1000 ppm concentration, which is not fatal for a human. The toxicity evaluation of the gases mixture within the whole quarry will be treated in the section 6.5.

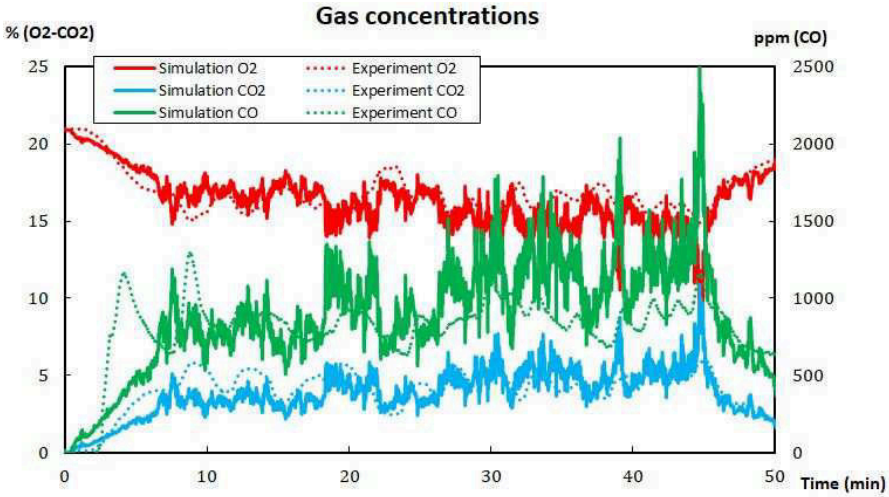

Fig. 19. Comparison between the numerical and experimental gases concentration at the point T2_1.

The simulation of the gases concentrations gives very satisfactory results. The dioxygen and the CO_2 are very well described and the average errors are 6% and 21% respectively. The experimental curves follow the numerical concentrations. The carbon monoxide is also similar to the experiment even if the gap between experiment and simulation is higher than the two others ($\varepsilon = 27\%$). It should be noted that the numerical results highly depend on the chemical reaction and the stoichiometric coefficients which were chosen to fit with the experimental results (section 3.4). Therefore, the range of the concentrations cannot be fully inaccurate. But the simulated trends are comparable with the measures and this point does not only stem from the stoichiometric coefficients. Indeed, the good description of the temperature at this point allows precise gases concentrations computations. A bad description of gases circulation would be a crippling handicap.

In the same way, we measured the soot concentration 18 cm below the ceiling at the point S1 (Fig. 3). Similarly, the simulated soot concentration is very accurate during all the combustion except at the beginning (Fig.20). It can be explained by the crossing of water vapor stemming from wood drying at the ignition. The amount of aerosols is large at the ignition of such wood fires. The establishment of the combustion takes time and the soot production is higher than for the rest of the fire. The simulation does not take this effect into account because the stoichiometric coefficient of soot remains constant. Excepting this spike, the simulation is conformed with the measures. Without considering the first five minutes, the average gap between simulation and experiment is 22%.

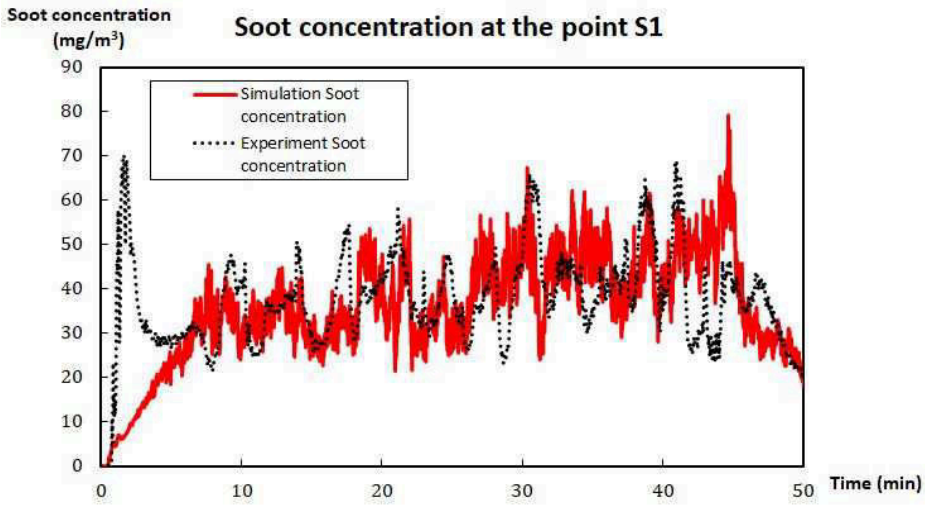

Fig. 20. Comparison between the numerical and experimental soot concentrations at the point S1.

The soot deposit comparison at two points (S1 and S2) reveals that simulation and experiment are not in the same order of magnitude, especially for the point S1 (Table 3):

Point	Experiment	Simulation
S1	0.84 mg	0.72 mg
S2	3.09 mg	0.54 mg

Tab. 3. Soot deposits at the points S1 and S2.

Several issues may explain the difference. First, the temperature gradient is very small near the wall. Therefore, the main processus of soot deposition could be another one than thermophoresis which is based on temperature gradient. Furthermore, the convective heat transfer is modeled from empirical formulations (see §4.1). The grid size is important in such a method as demonstrated in [58]. More generally, the inaccuracies could stem from the treatment of convective heat transfer to the walls. Estimating soot deposit on walls seems to require a precise method such as wall-resolved LES. As a result, we think that empirical formulations are not advanced enough to work out the soot deposition issue.

Nonetheless, this model informs about the smoke path during the combustion because of the borderline of the deposition (Fig. 21). It is an important matter for prehistorical fires because only the observation of soot deposit is possible. The numerical limit of deposition matches very well with the visual observation achieved after the end of the combustion.

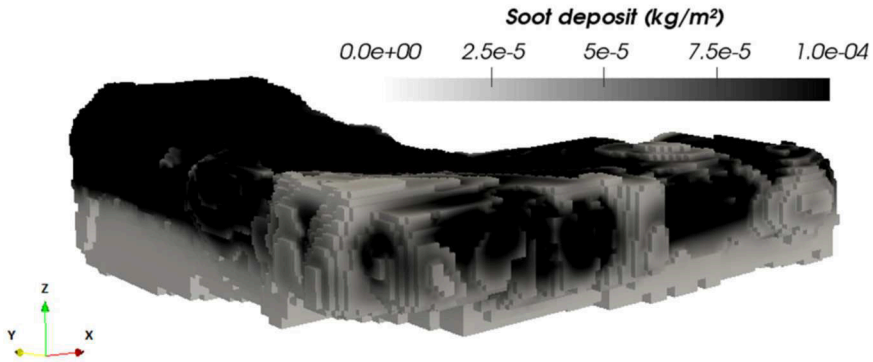

Fig. 21. Simulated soot deposit on the walls of the galleries.

6.4 Velocity

As previously mentioned in the section 2.2, two velocity sensors were placed at the entrance of the first gallery in order to measure the velocity in both layers. As expected, the velocity in the hot layer was higher than in the cold layer considering that the cold layer is larger with denser gases. The comparison with the numerical simulation is described on the figure 22.

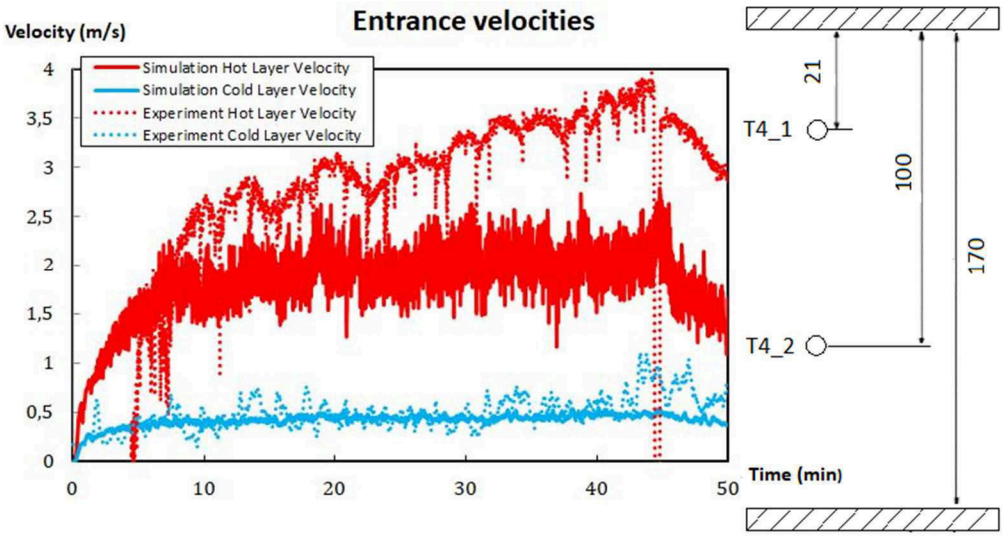

Fig. 22. On the left: comparison between the numerical and experimental velocities at the tree T4. On the right: cross section of the gallery near the tree T4, showing the vertical locations (in cm) of the velocity sensors.

The speed of outgoing flow is well simulated and the average is in the good range. Overall, the simulated cold layer velocity is in accordance with the experiments ($\varepsilon = 24\%$). However, at the end, a little error exists. Because of the HRR increase, the experimental velocity reaches a higher value. In the simulation, the upper velocity does not exceed 2.5 m/s. The experiment shows an increase until about 4 m/s at 45 minutes. This big gap ($\varepsilon = 36\%$) could be explained by the accumulation of inaccuracies from the fire to the entrance. The tree T4 is the farthest removed from the fire and consequently, it is the least accurate. This error could also be explained by the ceiling jet phenomenon. The sensor could be at the height of the maximum velocity. But the cells size in the hot layer is 6 cm. Hence, the simulation only gives an average of the hot layer velocity without being able to describe the velocity variation (see §4.1). The numerical velocity is then lower than the experimental one.

6.5 Fractional effective dose (FED)

The fractional effective dose for gases 50 minutes after the ignition is displayed on the figure 23.

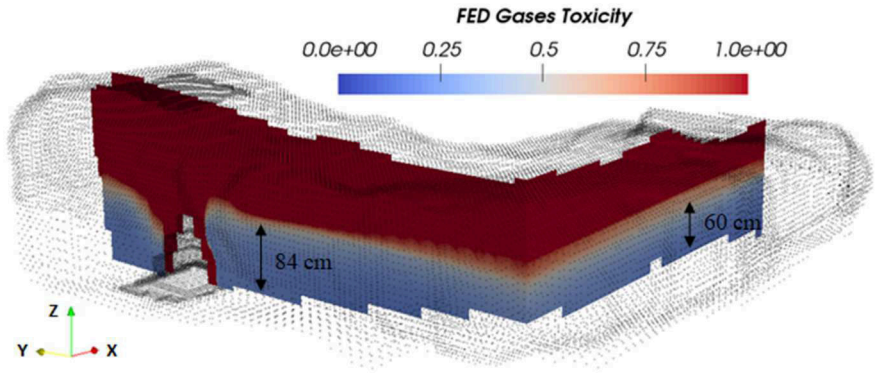

Fig. 23. Numerical estimation of the fractional effective dose for gases 50 minutes after the ignition in the median sections of both galleries.

As a reminder, half of people subjected to a FED of 1 are in the incapacity of leaving by themselves. So, the red color means that the location is very dangerous and may be lethal. But when the FED is worth 0.3, 11.4% of people cannot leave by themselves. Therefore, a great hazard is still present while the color is not clearly blue. The figure 23 shows the toxicity danger in the quarry during the experiment. Even close to the ground, everybody could risk serious trouble, fatal or not. This observation was expected because staying 50 minutes in such an environment is obviously unsafe.

The fractional effective dose for radiation and temperature 50 minutes after the ignition is displayed on the figure 24.

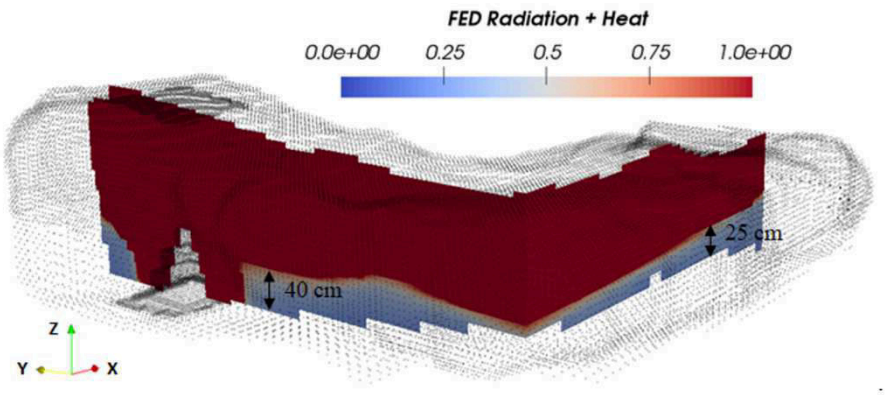

Fig. 24. Numerical estimation of the fractional effective dose for radiation and heat 50 minutes after the ignition in the median sections of both galleries.

Once again, the red color indicates a death rate of at least 50%. However, near the ceiling, the FED is far higher than 1. Being in this area definitely implies the death. In the gallery 1, even a person lying on the floor would be in the critical red area. Besides, within the whole quarry, the minimal value for this FED is 0.2. In any locations, the human presence is very unsafe and the intervention of the fire department to supply the hearth was absolutely legitimate.

An interesting point is the comparison between both FED. The radiation and the temperature in this experiment are more constraining than the toxicity. The gases are dangerous but for intense fires like these ones, the gases circulation is important and the toxic gases escape. In the cold area, the hazard exclusively stems from radiation because the temperature is cold enough to be bearable. Yet, the cold area is the safer location in such a fire. Therefore, radiation is the main threat that avoids human beings to remain in the galleries, close to the ground. The hot layer gases radiate too much energy to dwell on the floor without burning injuries. However, in confined caves, toxicity could be the main risk factor far enough from the fire, where prehistorical men could stay during the combustion.

7 Conclusion

Driven by archeological questions, an experiment is carried out in a former underground quarry. Three identical wood hearths are burned in order to test the reproducibility of such a combustion. The typical dimensions of the quarry make the results applicable to most of galleries, tunnels and mines. Various sensors are positioned throughout the gallery to measure gases and particles concentrations, temperatures and velocities. Some plates are fixed to the walls in order to collect the deposited soot. Then, the experimental measures are compared with the simulation performed by the numerical tool FireFOAM [22].

Three contributions have to be added to the program to get consistent results. First, a thermal boundary condition is needed to estimate the losses through the walls correctly. The ceiling jet phenomenon is modeled by an appropriate convective heat transfer estimation. Secondly, a thermocouple correction is implemented to compare measures with simulation aptly. A test case reveals a significant gap between the existing model and the implemented one which exactly gives the analytical solution. Finally, in light of the experimental results, an

assumption on the vertical velocity is required to simulate a meaningful solution. The velocity is considered exclusively horizontal outside the fire region except in the cells where the upper temperature is lower than the cell temperature. This enforcement suitably allows the simulation of two levels of stratification. This hypothesis seems to be valuable for the FireFOAM simulations of localized fires in confined geometries with opening.

The simulation of the experimental fire with FireFOAM is satisfactory. The comparison reveals a good agreement with the measures of temperatures, gases and particles concentrations. The velocity range of the cold layer also fits to the experiment. These results validate the modeling with FireFOAM and allow its application to the Chauvet-Pont d'Arc cave. The gap between simulation and experiment is small enough to characterize the fires of the Chauvet-Pont d'Arc cave efficiently.

In the purpose of improving the information about the environment, the soot deposition is estimated by the Beresnev-Chernyak model [49]. Even though the simulation does not successfully assess the amount of particles deposited on the quarry walls, the limits match with the visual observations. The hazard due to toxicity, radiation and temperature is calculated by means of the fractional effective dose (FED). In this study, the convection is efficient enough to evacuate gases and the greatest hazard turns out to be radiation. Therefore, the main hazard in a cavity such as the Chauvet-Pont d'Arc cave is likely radiation. This observation is of great importance for the supply of the hearth. Radiation is the more constraining danger in a gallery to supply the fireplace.

Great care should be given to the numerical heat release rate (HRR) in FireFOAM. The burner area has an important impact on the numerical HRR value. The mass flow rate imposed on the burner is not sufficient to ensure the same flow rate after the calculation of the species transport. In this simulation, we carefully design the hearth to provide the same HRR as the experimental one.

In the future, this modified version of FireFOAM will be used to simulate several fire scenarios in the Chauvet-Pont d'Arc cave. It should allow the discussion about the possible characteristics of these Paleolithic hearths. Afterwards, this modeling will be used in other archeological cavities with similar matters. Then, it could be used in more general contexts such as galleries, tunnels, mines or whichever comparable places.

8 Acknowledgements

We wish to thank the Regional Council of Aquitaine and Nouvelle-Aquitaine for providing funding for the CarMoThap project and for their investment in a 432-processor cluster located in the I2M laboratory. The researches in the Chauvet-Pont d'Arc cave have received specific financial help from the Ministry of Culture and Communication. We thank the LCPP (Laboratoire Centrale de la Préfecture de Police) for their help in the experiment instrumentation (velocity sensors, thermocouples, gases and particles concentrations). Furthermore, the following institutions have given support: CNRS, Bordeaux University, Bordeaux-Montaigne University. We thank C. Bouchet, the owner of the quarry in Fauroux

(Lugasson) and M. Vidal for having made available scots pine, as well as SDIS 33 staff for the participation in the experiments of the CarMoThaP program. We also express our gratitude to M. Corbé, L. Bassel, M. Bosq, E. Florensan, J. Sabidussi and C. Verdet for their precious help for wood packaging and their involvement in November 2016 experiments.

This work was also performed using HPC resources from GENCI-CINES (Grant 2017-A0032B10268).

9 References

[1] A. Trouvé and Y. Wan, "Large eddy simulation of compartment fires," *Intl. J. Comput. Fluid Dyn.,* vol. 24, pp. 449-466, 2010.

[2] S. Yuan et J. Zhang, «Large eddy simulation of compartment fire with solid combustibles,» *Fire Safety Journal,* vol. 44, n° 13, pp. 349-362, 2009.

[3] W. Zhang, A. Hamer, M. Klassen, D. Carpenter et R. Roby, «Turbulence statistics in a fire room model by large eddy simulation,» *Fire Safety Journal,* vol. 37, n° %18, pp. 721-752, November 2002.

[4] X. Zhang, Y. Guo, C. Chan et W. Lin, «Numerical simulations on fire spread and smoke movement in an underground car park,» *Building and Environment,* vol. 42, n° 110, pp. 3466-3475, 2007.

[5] X. Deckers, S. Haga, N. Tilley et B. Merci, «Smoke control in case of fire in a large car park : CFD simulations of full-scale configurations,» *Fire Safety Journal,* vol. 57, pp. 22-34, 2013.

[6] C. Hwang et J. D. Wargo, «Experimental study of thermally generated reverse stratified layers in a fire tunnel,» *Combustion and Flame,* vol. 66, n° 12, pp. 171-180, November 1986.

[7] J. S. Newman et A. Tewarson, «Propagation in Ducts,» *Combustion and Flame,* vol. 51, pp. 347-355, 1983.

[8] C. Caliendo, P. Ciambelli, M. D. Guglielmo, M. Meo et P. Russo, «Simulation of fire scenarios due to different vehicle types with and without traffic in a bi-directional road tunnel,» *Tunnelling and Underground Space Technology,* vol. 37, n° 11, pp. 22-36, 2013.

[9] W. Hsu, Y. Huang, T. Shen, C. Cheng et T. Chen, «Analysis of the Hsuehshan Tunnel Fire in Taiwan,» *Tunnelling and Underground Space Technology,* vol. 69, pp. 108-115, October 2017.

[10] J. Stenis et W. Hogland, «Fire in waste-fuel stores: risk management and estimation of real cost,» *Journal of Material Cycles and Waste Management,* vol. 13, n° 13, pp. 247-258, 2011.

[11] H. Wan, Z. Gao, J. Ji, Y. Zhang et K. Li, «Experimental and theoretical study on flame front temperatures within ceiling jets from turbulent diffusion flames of n-heptane fuel,» *Energy,* vol. 164, pp. 79-86, 2018.

[12] S. E. Zadeh, G. Maragkos, T. Beji et B. Merci, «Large Eddy Simulations of the Ceiling Jet Induced by the Impingement of a Turbulent Air Plume,» *Fire Technology,* vol. 52, n° 16, pp. 2093-2115, 2016.

[13] C.-S. Ahn, B.-H. Bang, M.-W. Kim, T.-G. Kim, S. C. James, A. L. Yarin et S. S. Yoon, «Numerical investigation of smoke dynamics in unconfined and confined environments,» *International Journal of Heat and Mass Transfer,* vol. 127, n° 1 Part B, pp. 571-582, 2018.

[14] A. Bordard, P. Guibert, C. Ferrier, E. Debard, B. Kervazo et J. Geneste, «Les rubéfactions des parois de la grotte Chauvet : une histoire de chauffe ?,» chez *Les arts de la Préhistoire : micro-analyses, mises en contextes et conservation, Paillet P. (dir)*, 2014.

[15] E. Debard, C. Ferrier et B. Kervazo, «Etude géologique de la grotte Chauvet-Pont d'Arc. Bilan des travaux de la triennale 2010-2012,» *Etudes pluridisciplinaires à la grotte Chauvet-Pont d'Arc (Ardèche). Rapport d'activité 2010-2012,* vol. 1, pp. 59-98, 2012.

[16] L. Liedgren, G. Hörnberg, T. Magnusson et L. Östlund, «Heat impact and soil colors beneath hearths in northern Sweden,» *Journal of Archaeological Science,* vol. 79, pp. 62-72, 2017.

[17] A. Quiles, H. Valladas, H. Bocherens, E. Delque-Kolic, E. Kaltnecker, J. v. d. Plicht, J.-J. Delannoy, V. Feruglio, C. Fritz, J. Monney, M. Philippe, G. Tosello, J. Clottes et J.-M. Geneste, «A high-precision chronological model for the decorate Upper Paleolithic cave of Chauvet-Pont d'Arc, Ardèche, France,» *Proceedings of the National Academy of Sciences,* vol. 113, n° 117, pp. 4670-4675, 2016.

[18] P. Guibert, A. Brodard, A. Quilès, J.-M. Geneste, D. Baffier, E. Debard et C. Ferrier, «When were the walls of the Chauvet Pont-d'Arc Cave heated ? A chronological approach by thermoluminescence,» *Quaternary Geochronology,* vol. 29, pp. 36-47, 2015.

[19] C. Ferrier, E. Debard, B. Kervazo, A. Brodard, P. Guibert, D. Baffier, V. Feruglio, B. Gely, J. Geneste et F. Maksud, «Les parois chauffées de la grotte Chauvet-Pont d'Arc (Ardèche): caractérisation et chronologie,» *Paléo,* vol. 25, pp. 59-78, 2014.

[20] D. Lacanette, J. Mindeguia, A. Brodard, C. Ferrier, P. Guibert, J. Leblanc, P. Malaurent

et C. Sirieix, «Simulation of an experimental fire in an underground limestone quarry for the study of Paleolithic fires,» *International Journal of Thermal Sciences,* vol. 120, pp. 1-18, 2017.

[21] K. McGrattan, S. Hostikka, R. McDermott, J. Floyd, C. Weinschenk et K. Overholt, «Fire Dynamics Simulator User's Guide, Sixth edition 1019,» NIST Special Publication, 2013. Available: https://pages.nist.gov/fds-smv/manuals.html.

[22] «FireFOAM,». Available: http://www.fmglobal.com/modeling.

[23] «OpenFOAM,». Available: http://www.openfoam.org/.

[24] G. Maragkos et B. Merci, «Large Eddy Simulations of CH4 Fire Plumes,» *Flow, Turbulence and Combustion,* vol. 99, n° 11, pp. 239-278, 2017.

[25] G. Maragkos, T. Beji et B. Merci, «Towards predictive simulations of gaseous pool fires,» *Proceedings of the Combustion Institute,* 2018 (in press).

[26] Y. Wang, P. Chatterjee et J. L. d. Ris, «Large eddy simulation of fire plumes,» *Proceedings of the Combustion Institute,* vol. 33, n° 12, pp. 2473-2480, 2011.

[27] S. Vilfayeau, N. Ren, Y. Wang et A. Trouvé, «Numerical simulation of under-ventilated liquid-fueled compartment fires with flame extinction and thermally-driven fuel evaporation,» *Proceedings of the Combustion Institute,* vol. 35, n° 13, pp. 2563-2571, 2015.

[28] D. Le, J. Labahn, T. Beji, C. B. Devaud, E. .. Weckman et A. Bounagui, «Assessment of the capabilities of FireFOAM to model large-scale fires in a well-confined and mechanically ventilated multi-cimpartment structure,» *Journal of Fire Sciences,* vol. 36, n° 11, pp. 3-29, 2018.

[29] G. Maragkos, T. Beji et B. Merci, «Advances in modelling in CFD simulations of turbulent gaseous pool fires,» *Combustion and Flame,* vol. 181, pp. 22-38, 2017.

[30] F. Salmon, C. Ferrier, D. Lacanette, J. Leblanc, J. Mindeguia et C. Sirieix, «Simulation numérique des feux et des thermo-altérations de la grotte Chauvet-Pont d'Arc (Ardèche),» chez *GMPCA*, Rennes, 2017.

[31] V. Dréan, G. Auguin, J.-C. Leblanc, D. Lacanette, J.-C. Mindeguia, A. Bellivier and C. Ferrier, "Numerical modelling of thermal conditions during fires in cave-like geometry," *Proceedings of the 15th International Conference Fire and Materials,* pp. 64-65, 2017.

[32] T. Lanki, J. Tikkanen, K. Janka, P. Taimisto et M. Lehtimäki, «An electrical sensor for long-term monitoring of ultrafine particles in workplaces,» *Journal of Physics: Conference Series,* vol. 304, n° 11, 2011.

[33] A. Bellivier, A. Coppalle, A. Loo, J. Yon, L. Decoster, S. Dupont et H. Bazin, «Comparison and Assessment of Particle Mass Concentrations Measurements in Fire Smokes with a Microbalance, Opacimeter and PPS Devices,» *10th AOSFST, October 5-7, 2015, Tsukuba, Japan.*

[34] M. Chase, «NIST-JANAF Thermochemical Tables, Fourth edition,» *Journal of Physical and Chemical Reference Data,* n° 1Mongraph No. 9, 1998.

[35] B. Poling, J. Prausnitz et J. O'Connell, The properties of gases and liquids, McGraw-Hill Education, 1987.

[36] W. Sutherland, «The viscosity of gases and molecular force,» *Philosophical Magazine,* vol. S. 5, pp. 507-531, 1893.

[37] A. Yoshizawa, «Statistical theory for compressible turbulent shear flows, with the application to subgrid modeling,» *Physics of Fluids,* vol. 29, n° 17, pp. 2152-2164, 1986.

[38] V. Tihay, Y. Perez-Ramirez, F. Morandini, P. Santoni et T. Barboni, «Heat transfers and energy released in the combustion of fine vegetation fuel beds,» *21ème Congrès Français de mécanique,* 2013.

[39] W. Grosshandler, «A Narrow-Band Model for Radiation Calculations in a Combustion Environment,» *NIST Technical Note 1402,* 1993.

[40] S. Sazhin, «An Approximation for the Absorption Coefficient of Soot in a Radiating Gas,» *Manuscript, Fluent Europe,* 1994.

[41] B. Magnussen et B. Hjertager, «On mathematical modeling of turbulent combustion with special emphasis on soot formation and combustion,» *Proc. Combust. Int,* pp. 719-729, 1977.

[42] C. Verdet, Y. Anguy, C. Sirieix, R. Clément et C. Gaborieau, «On the effect of electrode finitnessin small scale electrical resistivity imaging,» *Geophysics,* 2018.

[43] C. Bonacina, G. Comini, A. Fasano et M. Primicerio, «Numerical solution of phase-change problems,» *Int J Heat Mass Transf,* vol. 16, pp. 1825-1832, 1973.

[44] R. Alpert, SPFE Handbook of Fire Protection Engineering, Chapter Ceiling Jet Flows, National Fire Protection Association, Quincy, Massachusetts, fourth edition, 2008.

[45] J. Holman, Heat Transfer, New York: McGraw-Hill, 7th edition, 1990.

[46] Y. Jaluria et L. Cooper, «Negatively buoyant wall flows generated in enclosure fires,» *Progress in Energy and Combustion Science,* vol. 15, pp. 159-182, 1989.

[47] L. Cooper, «Ceiling Jet-Driven Wall Flows in Compartment Fires,» *Combustion Science and Technology,* vol. 62, n° 14-6, pp. 285-296, 1988.

[48] L. Cooper, «Ceiling Jet Properties and Wall Heat Transfer in Compartment Fires Near Regions of Ceiling-Jet Wall Impingement,» *National Bureau of Standards NBSIR,* Vols. 1 sur 286-3307, 1986.

[49] S. Beresnev et V. Chernyak, «Thermophoresis of s spherical particle in a rarefied gas: Numerical analysis based on the model kinetic equations,» *Physics of Fluids,* vol. 7, pp. 1743-1756, 1995.

[50] B. Sagot, G. Antonini et F. Buron, «Annular flow configuration with high deposition efficiency for the experimental determination of thermophoretic diffusion coefficients,» *Journal of Aerosol Science,* vol. 40, n° 112, pp. 1030-1049, 2009.

[51] E. Brugière, *PhD thesis,* INSA (Rouen), 2012.

[52] D. Purser et J. McAllister, SPFE Handbook of Fire Protection Engineering, chapter Assessment of Hazards to Occupants from Smoke, Toxic Gases, and Heat, Springer, 2016.

[53] L. Speitel, «Fractional effective dose model for post-crash aircraft survivability,» *Toxicology,* vol. 115, pp. 167-177, 1996.

[54] D. Purser, «Physiological effects of combustion products and fire hazard assessment,» *Europacable Seminar "Safety during Fire",* 6 May 2009.

[55] «OpenFOAM-Thermocouple». Available: https://www.openfoam.com/releases/openfoam-v1612+/post-processing.php.

[56] R. Peacock, W. Jones, R. Bukowski et G. Forney, «CFAST-Consolidated Model of Fire Growth and Smoke Transport (Version 6) Technical Reference Guide,» 2005.

[57] «SnappyHexMesh». Available: https://openfoam.org/?s=snappyhexmesh.

[58] K. Overholt, J. Floyd et O. Ezekoye, «Computational Modeling and Validation of Aerosol Deposition in Ventilation Ducts,» *Fire Technology,* vol. 52, pp. 149-166, 2016.

Figure captions

Fig. 1. 3D geometry of the quarry acquired by photogrammetry (P. Mora, Archéotransfert).

Fig. 2. On the left: Initial hearth in a tepee configuration at the back of the gallery 2. The wood is placed on a weighing scale. On the right: Wood supply by firemen with security equipment.

Fig. 3. Cut-away view of the quarry with the locations of the hearth, the thermocouples trees and the soot deposit measures. A camera was placed on the floor, near the corner. Dimensions are in cm.

Fig. 4. Comparison between theoretical and simulated temperature profiles close to the ceiling.

Fig. 5. Schematic representation of the ceiling jet-driven wall flows phenomenon (without penetration in the cold layer).

Fig. 6. Evolution of a thermocouple response in a simple test case, calculated with the existing model and the new implemented one. Both models are compared to the analytical solution.

Fig. 7. On the left: measured temperature at the tree T1 at the points T1_1 and T1_2. On the right: cross section of the gallery near the tree T1, showing the vertical location (in cm) of the thermocouples.

Fig. 8. On the left: numerical temperature field in the median section of the second gallery 20 minutes after the ignition of the combustion. On the right: simulated temperature at the tree T1 at the points T1_1 and T1_2.

Fig. 9. Schematic representation of the horizontal velocity hypothesis. The enforcement is only applied far enough from the fire.

Fig. 10. On the left: numerical temperature field in the median section of the second gallery 20 minutes after the ignition of the combustion. On the right: simulated temperature at the tree T1 at the points T1_1 and T1_2. Both are performed without z-velocity outside the turning region.

Fig. 11. 3D mesh of the quarry performed by the tool snappyHexMesh [57].

Fig. 12. 3D mesh of the hearth at the back of the gallery 2 with plate burners (black color).

Fig. 13. 3D geometry of the test case corresponding to a cube. The plate burner is the black square (variable size depending on the configuration).

Fig. 14. Comparison between the numerical heat release rates of the four configurations. The dashed line corresponds to the theoretical HRR.

Fig. 15. Comparison between the numerical and the experimental HRR (Heat Release Rates).

Fig. 16. On the left: comparison between the numerical and experimental temperatures at the tree T1. On the right: cross section of the gallery near the tree T1, showing the vertical locations (in cm) of the thermocouples.

Fig. 17. On the left: comparison between the numerical and experimental temperatures at the tree T2. On the right: cross section of the gallery near the tree T2, showing the vertical locations (in cm) of the thermocouples.

Fig. 18. On the left: comparison between the numerical and experimental temperatures at the tree T3. On the right: cross section of the gallery near the tree T3, showing the vertical locations (in cm) of the thermocouples.

Fig. 19. Comparison between the numerical and experimental gases concentration at the point T2_1.

Fig. 20. Comparison between the numerical and experimental soot concentrations at the point S1.

Fig. 21. Simulated soot deposit on the walls of the galleries.

Fig. 22. On the left: comparison between the numerical and experimental velocities at the tree T4. On the right: cross section of the gallery near the tree T4, showing the vertical locations (in cm) of the velocity sensors.

Fig. 23. Numerical estimation of the fractional effective dose for gases 50 minutes after the ignition in the median sections of both galleries.

Fig. 24. Numerical estimation of the fractional effective dose for radiation and heat 50 minutes after the ignition in the median sections of both galleries.

Table captions

Tab. 1. Moments of supply and corresponding added masses.

Tab. 2. Plate buner areas for each configuration.

Tab. 3. Soot deposits at the points S1 and S2.